

Exploring Electronic Properties Of Twisted Bilayer Graphene



S Ramachandra Bangari

Undergraduate Programme

Department of Instrumentation and Applied Physics

Indian Institute of Science

Submitted in partial fulfillment of the requirements for the
Degree of Bachelor of Science (Research)
in Physics

Supervisor

Dr. Chandni U,
Department of Instrumentation and Applied Physics,
Indian Institute of Science

June 2021

Declaration

I certify that -

- (a) The work contained in this report has been done by me under the guidance of my supervisor.
- (b) The work has not been submitted to any other Institute for any degree or diploma.
- (c) I have conformed to the norms and guidelines given in the Ethical Code of Conduct of the Institute.
- (d) Whenever I have used materials (data, theoretical analysis, figures, and text) from other sources, I have given due credit to them by citing them in the text of the thesis and giving their details in the references.

Date - 30 June, 2021

S Ramachandra Bangari

Place - IISc, Bangalore

11-01-00-10-91-16-1-14477

UNDERGRADUATE PROGRAMME
INDIAN INSTITUTE OF SCIENCE
BANGALORE - 560012, INDIA



CERTIFICATE

This is to certify that the Bachelor's thesis entitled "**Exploring Electronic Properties Of Twisted Bilayer Graphene**" submitted by **S Ramachandra Bangari** (Sr No. 11-01-00-10-91-16-1-14477) to Indian Institute of Science, Bangalore towards partial fulfilment of requirements for the award of degree of Bachelor of Science (Research) in Physics is a record of bona fide work carried out by him under my supervision and guidance during Academic Year, 2020-21.

Date - 30 June, 2021

Dr. Chandni U

Place - IISc, Bangalore

Dept. of Instrumentation and Applied Physics

Indian Institute of Science
Bangalore - 560012, India

Abstract

Twisted bilayer graphene (twBLG) has emerged as a highly tunable platform for studying strong electronic correlations. Transport measurements in magic angle twBLG have shown that it exhibits correlated insulator states, superconductivity, ferromagnetism and quantum anomalous Hall effect. Tunneling measurements throw light on the band structure and help understand the scattering processes in a two-dimensional electron gas. In this thesis, we discuss the fabrication of twBLG heterostructure for tunneling. We perform transport measurements in the device and find it has a low twist angle between the graphene layers.

Acknowledgements

I would like to thank everyone that helped me through my journey of exploring physics. This project wouldn't have been possible without the guidance from my supervisor, Dr. Chandni U., who has shown me the path of research with her expertise. I am thankful to Radhika for fruitful discussions and advice, and all my labmates, Mrityunjay, Pragya, Manjari, Saisab, Suvronil, who helped me at every step of my way.

I am grateful to my friends, who made my stay at IISc enjoyable: abeliangoop, sideart, eps1lon, rahul, anish, takenpuppet, kababsingh, shinespark31, resq, aniket, rainbowtotem, cyanide, poorjoke, harlequin, hawk, altair177, kruthi, rimika, ashish, to name a few. I also thank my family for their support.

I am very fortunate to have spent my eventful years at IISc, which gave me an amazing environment for studying science and introduced me to many new things, shaping who I am today.

Contents

1	Introduction	1
1.1	Motivation	1
1.2	Overview	2
2	Theory	4
2.1	Graphene	4
2.2	Bilayer graphene	7
2.3	Twisted bilayer graphene	9
2.3.1	Moiré superlattices	9
2.3.2	Continuum model developed by MacDonald	10
2.3.3	Flat bands in twBLG	15
2.3.4	Experimental signatures of twBLG	17
2.4	Tunneling	22
3	Methods	30
3.1	Exfoliation of graphene and hBN	31
3.2	Flake selection	35
3.2.1	Optical microscope	35
3.2.2	Raman spectroscopy	36
3.2.3	Atomic force microscopy	39
3.3	Stamp creation	40
3.4	Pickup and transfer process	42
3.5	Twisted bilayer graphene stack	48
4	Measurements	51
4.1	Sample insertion and instruments used	51
4.2	Checking contacts	52
4.3	Checking gate leakage	54
4.4	Transport measurement	54
4.5	Tunneling measurement	56

4.6	Stack 62	57
4.6.1	Checking contacts and gate leakage	59
4.6.2	Transport measurements and results	60
5	Conclusions	65
5.1	Summary	65
5.2	Future work possible	65

List of Figures

2.1	Graphene Lattice and its Brillouin zone. Left: Two interpenetrating triangular lattices forming graphene honeycomb lattice. a_1 and a_2 are lattice vectors and $\delta_i, i = 1, 2, 3$ are the nearest neighbour vectors. Right: Corresponding Brillouin zone that shows high symmetry points. The Dirac cones are located at K and K' points. Figure adapted from [28] .	4
2.2	Electronic dispersion of graphene. Left: Energy spectrum of the honeycomb lattice in units of t for non zero t and t' . Here $t = 2.7eV$ and $t' = -0.2t$. Right: Zoom in of the energy bands near one of the Dirac points. Figure adapted from [28]	6
2.3	Bernal stack bilayer graphene lattice with hopping terms and its Brillouin zone. Left: Two monolayer graphene in AB stacking forming bernal stack bilayer graphene lattice. $\gamma_0, \gamma_1, \gamma_3$ and γ_4 are the hopping terms. Right: Corresponding Brillouin zone that shows high symmetry points. Figure adapted from [28]	7
2.4	Electronic dispersion of bilayer graphene when $\Delta = 0$ (left) and $\Delta \neq 0$ (right). A band gap Δ_g opens up in the presence of an external displacement field. Figure adapted from [29]	9
2.5	twBLG Moiré pattern and its mini Brillouin zone. Left: The Moiré pattern as seen in twBLG. The Moiré wavelength is $\lambda = \frac{a}{2\sin(\theta/2)}$. Right: The mini Brillouin zone is constructed from the difference between the two $K(K')$ wavevectors for the two layers. K_s, K'_s, M_s and Γ_s denote points in the mini Brillouin zone. Figure adapted from [1]	10

2.6 twBLG in momentum space (A) Dashed line marks the first Brillouin zone of an unrotated layer. The three equivalent Dirac points are connected by $\mathcal{G}^{(2)}$ and $\mathcal{G}^{(3)}$. The circles represent Dirac points of the rotated graphene layers, separated by $k_\theta = 2k_D \sin(\theta/2)$, where k_D is the magnitude of the Brillouin-zone corner wave vector for a single layer. (B) The three equivalent Dirac points in the first Brillouin zone result in three distinct hopping processes. For all the three processes $ q_j = k_\theta$. The green solid line marks the Moiré band Wigner–Seitz cell. The red and black circles mark the Dirac points of the two layers. Figure adapted from [17]	11
2.7 Moiré bands (A) Energy dispersion plotted along A-B-C-D-A (see fig. 2.6), for bands closest to the Dirac point. (B) Density of states. (C) Energy as a function of twist angle for the $k = 0$ states. (D) Full dispersion of the flat band at $\theta = 1.05^\circ$. Figure adapted from [17]	14
2.8 Renormalized Dirac-point band velocity. The band velocity of the twBLG at the Dirac point plotted against α^2 , where $\alpha = w/vk_\theta$. Inset shows renormalised velocity at large twist angles. Figure adapted from [17] . .	15
2.9 Electronic band structure of twBLG	16
2.12 twBLG transport signatures. Top: Four-terminal longitudinal resistance plotted against carrier density at different perpendicular magnetic fields from 0 T (black trace) to 480 mT (red trace). Bottom: Colour plot of longitudinal resistance against carrier density and temperature, showing different phases including metal, band insulator (BI), correlated state (CS) and superconducting state (SC). Figure adapted from [32]	20
2.13 (A) Magnetic field dependence of the longitudinal resistance R_{xx} (upper panel) and Hall resistance R_{yx} (lower panel) at 30 mK, showing a hysteretic AH effect resulting from emergent magnetic order. (C) Temperature dependence of R_{yx} versus B between 46 mK and 5.0 K, showing the hysteresis loop closing with increasing temperature. Figure adapted from [5]	21
2.14 (C) R_{xy} as a function of B and n. The rear wall shows field-training symmetrized values of R_{xy} at B = 0. Zero-field anomalous Hall signal becomes nonzero when ferromagnetism appears, and it reaches a plateau of h/e^2 . (D) Schematic band structure at filling factors 4 and 3. The net Chern number is 1 at filling factor 3. Figure adapted from [4]	22

2.15 (a) Graphene-hBN-graphene device structure. (b) A rotation by θ of the two graphene layers in real space corresponds to the momentum shift K_i^\pm between two Dirac points. (c,e,f) Relative alignment between the top (left cones) and bottom (right cones) graphene Dirac points. The boundary between magenta (empty states) and blue (filled states) marks the Fermi level. Figure adapted from [6]	23
2.16 (a) Current density vs voltage curves at different gate voltages. (b) Conduction plots as a function of gate and bias voltage. Figure adapted from [6]	23
2.17 (b) Trajectories of the charged quasiparticles tunneling from top to bottom graphene layers in zero and finite magnetic fields caused by the Lorentz force. (c) dI/dV maps measured with a 15 T in-plane magnetic field applied. (e) Difference between the dI/dV maps with and without the in-plane magnetic field. Figure adapted from [6]	24
2.18 Interlayer current-voltage characteristics at (a) 10 K and (b) room temperature in double bilayer graphene - hBN. (c) Normalized interlayer resistance vs number of hBN layers measured in multiple devices and at a low temperature of T = 1.4-20 K and at room temperature. Figure adapted from [24]	24
2.19 Energy band alignment and carrier densities at tunneling resonance in double bilayer graphene - hBN. (a) Energy band diagram of double bilayer graphene when charge neutrality points of top and bottom bilayers are aligned. (b) Interlayer bias vs back gate voltage at tunneling resonance (circles and squares) and when charge neutrality points are aligned (solid line) (c) Carrier densities of top and bottom layer at resonance tunneling. Figure adapted from [24]	25
2.20 Different contributions to the total interlayer tunneling current in double bilayer graphene - WSe ₂ . (a) Calculated interlayer tunneling current versus interlayer bias at top gate voltage -2 V and T = 1.5 K. The simulated data shows the total interlayer tunneling current (black), along with the like- (red) and unlike-band (green) tunneling. The symbols represent corresponding experimental data. (b) Energy band-alignment of the top (red) and bottom (green) graphene bilayers at various bias voltages. The dashed red (green) line marks the chemical potential of the top (bottom) graphene bilayer. Figure adapted from [25]	25

2.21 Experimental (a) and calculated (b) interlayer conductivity vs interlayer bias and top gate voltage at back gate voltage -20 V and T = 1.5 K, in double bilayer graphene - WSe_2 . The points labeled in (b) identify distinct tunneling regimes. (c) Energy band alignment of top (red) and bottom (blue) bilayer graphene bands corresponding to the biasing conditions labeled in (b). The dashed lines mark the two layer Fermi levels. Figure adapted from [26]	26
2.22 (a) Band diagram of an isolated graphene and metal system. (b) Band diagram of a Metal-Graphene (MG) junction at equilibrium showing dipole formation at the interface. (c) Nonequilibrium band diagram of the MG junction. Figure adapted from [27]	27
2.23 Schematic representation of the tunneling current between graphene and metal electrodes. Figure adapted from [27]	27
2.24 Tunneling measurements done in devices with two GaAs quantum wells separated by a $Al_{0.33}Ga_{0.67}As$ barrier. Figure adapted from [7]	28
2.25 Side-view of the Fermi surfaces of graphene and metal showing two possible phonon modes that contribute to tunneling. Figure adapted from [8]	29
 3.1 The device structure that is required in twisted bilayer graphene tunneling experiment.	30
3.2 Conventional exfoliation process. Figure adapted from [39]	32
3.3 Heater at lab that has a hot plate used during exfoliation.	32
3.4 Plasma cleaner setup at lab.	33
3.6 Optical microscope at the lab used to find the flakes.	35
3.7 hBN flake showing regions with varying thickness.	36
3.8 (a) Raman spectra of single layer graphene and bulk graphite at 514 nm showing G peak (left) and 2D peak (right). (b,c) Evolution of Raman spectra at 514 nm with number of graphene layers at 514 nm and 633 nm. (d) D band at the edge of single layer graphene and bulk graphite at 514 nm. (e) The four components of the 2D band in 2 layer graphene at 514 and 633 nm. Figure adapted from [42]	37
3.9 Raman spectra of hBN of varying thickness. The left inset show changes in integrated intensity with the number of layers N. The right picture illustrates the phonon mode responsible for the Raman peak. Figure adapted from [44]	38

3.10 AFM of 5nm hBN flake. Top right: Optical image of the flake. Top left: AFM mapping of the flake, to find cleanliness. Bottom: Thickness of hBN flake as a function of position taken along the line shown in the top left figure.	39
3.11 A coverslip with PDMS on it.	40
3.12 Sonicator and spin coater at lab.	41
3.13 Schematic of pickup and transfer process used in making twisted bilayer graphene stack for tunneling measurement: Part 1.	42
3.14 Schematic of pickup and transfer process used in making twisted bilayer graphene stack for tunneling measurement: Part 2.	43
3.15 Transfer Setup at lab.	45
3.16 Pickup and Transfer of thin hBN on gold pad (bottom tunneling electrode). .	48
3.17 Pt-Ir tip that is used in cutting graphene flake and Pt-Ir wire.	49
3.18 Making hBN-graphene-graphene stack on PPC.	50
 4.1 Sample insertion.	51
4.2 Instruments used at lab.	52
4.3 Circuit diagram for checking contacts in the sample. LIA is Lock-in amplifier that provides an AC signal of 1 V and 13 Hz. It is connected to a voltage divider, followed by a resistor which is connected to the contact that needs to be checked (other contacts are grounded). Points A and B are connected to LIA input to measure the voltage across the resistor. .	53
4.4 Circuit diagram for transport measurements in the sample. LIA is Lock-in amplifier that provides AC signal of 1 V and 13 Hz. It is followed by a resistor connected to the source of the sample, whose drain is grounded. Back (top) gate (G1) is connected to a sourcemeter to control the gate voltage, while top (back) gate (G2) is set to a constant value using another sourcemeter. Voltage across two twBLG/hall contacts in the sample is measured by LIA.	55
4.5 Circuit diagram for tunneling measurements in the sample. LIA is a Lock-in amplifier that provides an AC signal of $V_{LIA} = 5$ V and 13 Hz. It is followed by a voltage divider connected to a transformer. DC voltage is supplied by Kepco sourcemeter that adds to the AC voltage coming from the transformer. The AC+DC voltage is supplied to the sample through a tunnel contact T. A hall contact of the sample is then connected to LIA and a digital multimeter (DVM) through a pre-amplifier.	57

4.6	Optical image of stack 62 at 5x magnification. The scale on the right is 200 μm . All the contacts are numbered. S, D and TG represent source, drain and top gate, respectively. H1, H1', H2, H3 represent twBLG/hall contacts. T1 and T2 represent tunnel contacts. 1 and 13 are back gate contacts (not shown here as they are contacts with substrate directly).	58
4.7	Optical image of stack 62 at 100x magnification. The scale on the right is 10 μm . The nomenclature is the same as in fig. 4.6	59
4.8	Data for checking contacts	59
4.9	Resistance vs carrier density for different contact pairs. Back gate is set to 0 V and top gate is swepted between -5 V and 5 V.	61
4.10	Resistance vs top gate voltage for contact pair (5,6) at different back gate voltages.	62
4.11	Resistance vs top gate voltage for contact pair (6,8) at different back gate voltages.	62
4.12	The dependence of the longitudinal resistance on top and bottom gate in (a) Bernal-stacked BLG, (b) large-angle TBG (2.8°) and (c) small-angle TBG (0.47°). The insets in the top right corner show several line cuts at fixed top-gate voltages. Schematic band structures in the inset show how the band structures change as a function of the perpendicular electric displacement field, D. The schematic diagram of the triangular network of resistors in (c) represents the current paths generated along the domain boundaries obtained by gapping out AB and BA domains with transverse electric field. DB denotes the domain boundaries. Figure adapted from [46]	64

Chapter 1

Introduction

1.1 Motivation

There has been a great deal of interest in twisted Moiré superlattice since the discovery of correlated insulating states and superconductivity in magic angle twisted bilayer graphene (twBLG). [1] [2] This gave rise to a new field called “twistronics”. [3] This is a new platform hosting strong electron correlations, providing an alternative for understanding unconventional superconductivity. Transport measurements show us the different phases exhibited by twBLG due to strong correlation, including ferromagnetism and quantum anomalous Hall effect. [4, 5] Tunneling measurements shed some light on the band structure of the material involved, and hence can be a great probe in digging deep into this feature-rich heterostructure. [6] They also help in finding the lifetime of the electrons within a two-dimensional electron gas (2DEG), which gives information about the scattering processes involved. [7] From the width of the tunneling resonance, the lifetime of the electrons within a 2DEG can be calculated, which tells us about the density dependence of the electron-impurity scattering and the temperature dependence of the electron-electron scattering. Phonon-assisted tunneling is also possible where phonons can provide the momentum needed to overcome the Fermi surface mismatch and allow tunneling. [8]

1.2 Overview

An electron in a crystal is subjected to a periodic potential, obeying dispersion from band structure in reciprocal space. In superlattices, the secondary larger periodic potential breaks the reciprocal space by introducing miniband structures. Fabricating an artificial superlattice is difficult in a common crystal. However, in a two-dimensional (2D) system like graphene, it is easy to create superlattice just by twisting two layers, [9, 10, 11, 12, 13, 14] giving rise to Moiré superlattice with a long wavelength, shown by developments in 2D van der Waals heterostructures. [15]

For example, the long-periodical potential in graphene/hexagonal boron nitride (hBN) Moiré superlattice reshapes the linear band structure by producing superlattice minibands, leading to the observations of fractal Hofstadter butterfly spectrum and satellite secondary insulating states. [16]

Unlike graphene/hBN heterostructure, twisted bilayer graphene is able to tune not only the size of the Moiré band but also the electronic coupling between the two layers. This changes a single particle non-interacting picture to a many-body interacting picture. It was predicted that the electronic Fermi velocity almost vanishes around zero Fermi energy at a discrete set of angles. [17] At these “magic angles”, flat bands are formed that lead to correlation effect dominated electronic behaviour when the bandwidth is smaller than the Coulomb repulsion energy. We will discuss more about the theory in section 2

Despite the prediction of the magic angle in 2011, such magic-angle samples were not experimentally realised until 2018. The first and biggest challenge is the accurate control of the twist angle while fabricating the heterostructure. The breakthrough was the development of the ‘tear and stack’ technique, [18] which involves tearing a single flake of graphene into two by an hBN flake and picking up one of them, then rotating the bottom graphene flake by an angle and picking it up. We will discuss more about the methods used in fabricating twBLG in section 3.

Another problem is the dynamic instability of a small angle in the twisted

bilayer graphene after the transfer. Since the most energetically stable stacking is Bernal or AB stacking, i.e., zero twist angle, magic angle samples with a twist of 1.1° [17] will tend to decrease to zero upon application of strain, heat, etc. [19, 20]

Renormalisation of Fermi velocity, [21, 22, 23] insulating states at the superlattice band edges [21] and satellite Landau fans were observed [14, 21] even before the magic angle samples were realised. They indicated the possibility of exotic phenomena near magic angle, even though they didn't show any. Eventually, Pablo Jarillo-Herrero's group at MIT could obtain magic angle samples and observe the correlated insulating states and superconductivity. [1, 2] We will discuss the signatures of twBLG in section 2.3.4.

Some works on tunneling measurements were done parallelly on graphene-insulator-graphene and bilayer graphene-insulator-bilayer graphene. [6, 24, 25, 26] We will discuss them in section 2.4, along with tunneling in graphene-insulator-metal heterostructure. [27]

We will discuss the protocols for measurement and results from the twBLG device we measured in section 4. The signatures suggest that our device has a low twist angle between the graphene layers.

Chapter 2

Theory

2.1 Graphene

Graphene is a monolayer of carbon atoms arranged in a honeycomb lattice that can be thought of as two interpenetrating triangular sublattices with two nonequivalent carbon atoms.

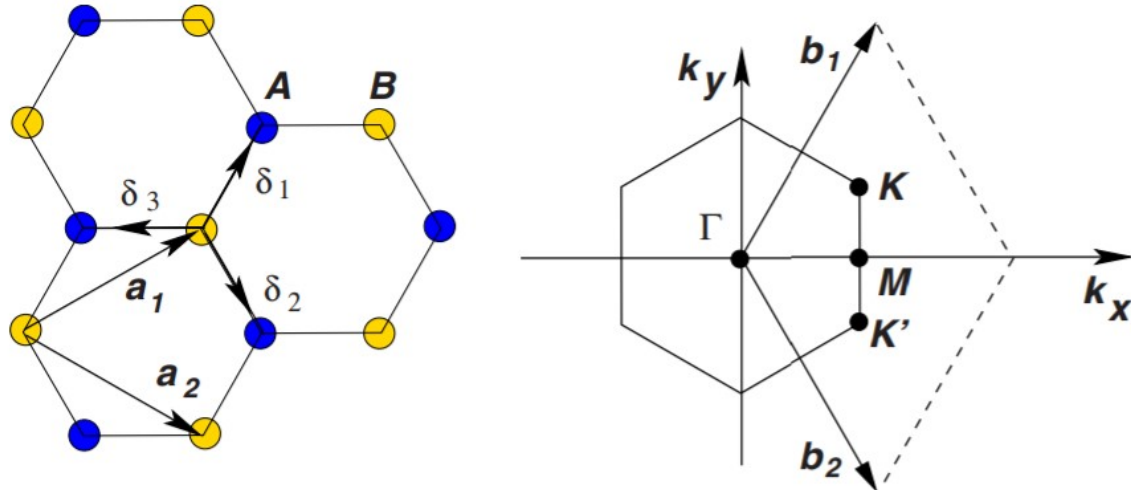


Figure 2.1: Graphene Lattice and its Brillouin zone. Left: Two interpenetrating triangular lattices forming graphene honeycomb lattice. a_1 and a_2 are lattice vectors and $\delta_i, i = 1, 2, 3$ are the nearest neighbour vectors. Right: Corresponding Brillouin zone that shows high symmetry points. The Dirac cones are located at K and K' points. Figure adapted from [28]

The primitive lattice vectors for the lattice are given by (see fig. 2.1):

$$a_1 = \frac{a}{2}(3, \sqrt{3}), a_2 = \frac{a}{2}(3, -\sqrt{3}) \quad (2.1)$$

The reciprocal lattice vectors are given by (see fig. 2.1):

$$b_1 = \frac{2\pi}{3a}(1, \sqrt{3}), b_2 = \frac{2\pi}{3a}(1, -\sqrt{3}) \quad (2.2)$$

The wave vectors of the high symmetry points in the first Brillouin zone are given below, where K and K' are two nonequivalent corners known as the Dirac points, as shown in fig. 2.1.

$$\Gamma = (0, 0), K = \frac{2\pi}{3a}(1, \frac{1}{\sqrt{3}}), K' = \frac{2\pi}{3a}(1, -\frac{1}{\sqrt{3}}), M = \frac{2\pi}{3a}(1, 0) \quad (2.3)$$

The electronic structure of graphene can be derived using the tight binding model, considering nearest and next nearest neighbour hopping. The Hamiltonian becomes:

$$H = -t \sum_{<ij>, \sigma} (a_{\sigma,i}^\dagger b_{\sigma,j} + H.c) - t' (a_{\sigma,i}^\dagger a_{\sigma,j} + b_{\sigma,i}^\dagger b_{\sigma,j} + H.c.) \quad (2.4)$$

where $a_{\sigma,i}$, $a_{\sigma,i}^\dagger$ and $b_{\sigma,i}$, $b_{\sigma,i}^\dagger$ are the annihilation and creation operators on site A and B, with spin σ , respectively. t is the nearest neighbour hopping energy $\approx 2.7\text{eV}$ and t' is the next nearest neighbour hopping energy $\approx -0.2t$. We can diagonalise the Hamiltonian and derive the electronic dispersion to be [28]:

$$E_\pm(\mathbf{k}) = \pm t\sqrt{f(\mathbf{k}) + 3} - t'f(\mathbf{k}), f(\mathbf{k}) = \cos(\frac{\sqrt{3}}{2}k_y a)\cos(\frac{3}{2}k_x a) + 2\cos(\sqrt{3}k_y a) \quad (2.5)$$

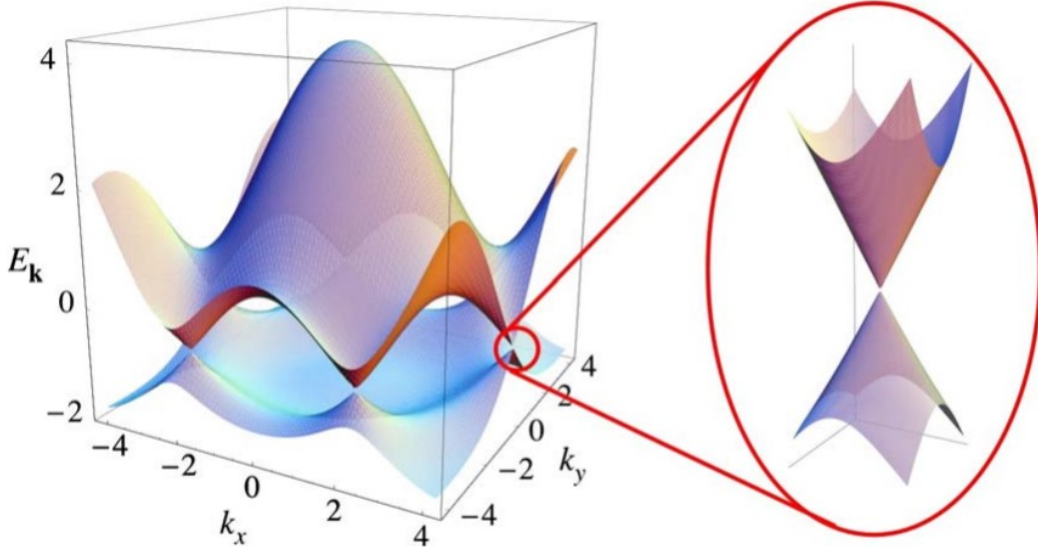


Figure 2.2: Electronic dispersion of graphene. Left: Energy spectrum of the honeycomb lattice in units of t for non zero t and t' . Here $t = 2.7\text{eV}$ and $t' = -0.2t$. Right: Zoom in of the energy bands near one of the Dirac points. Figure adapted from [28]

This gives a symmetric band structure for holes and electrons around zero energy, if we take t' to be zero. But the electron-hole symmetry is broken and the upper and lower bands become asymmetric for finite next nearest neighbour hopping. In fig. 2.2, the full band structure of graphene is shown. A zoom in of the band structure close to one of the Dirac points is also shown. This dispersion can be obtained by expanding the full band structure, close to \mathbf{K} or \mathbf{K}' vector, i.e., $\mathbf{k} = \mathbf{K} + \mathbf{q}$ ($|\mathbf{q}| \ll |\mathbf{K}|$):

$$E_{\pm}(\mathbf{q}) = \pm v_F |\mathbf{q}| + O[(q/K)^2] \quad (2.6)$$

where \mathbf{q} is the momentum measured relatively to the Dirac points and v_F is the Fermi velocity, given by $v_F = 3ta/2$.

The above equation shows that the energy bands linearly cross at the Dirac points, and hence the graphene acts as a zero band gap material with a linear dispersion. The approximation is valid for small carrier densities. From equation (2.6), the Hamiltonian near the Dirac points can be written as:

$$H_{Dirac} = \begin{bmatrix} 0 & q_x - iq_y \\ q_x + iq_y & 0 \end{bmatrix} = v_F \sigma \cdot \mathbf{q} \quad (2.7)$$

where σ is the corresponding Pauli matrices. This is equivalent to the equation for massless chiral Dirac fermions in 2D where the speed of light has been replaced by v_F and with a pseudospin spinor structure related to the graphene sublattices. Many of the interesting properties of graphene can be explained using this unique and interesting dispersion.

2.2 Bilayer graphene

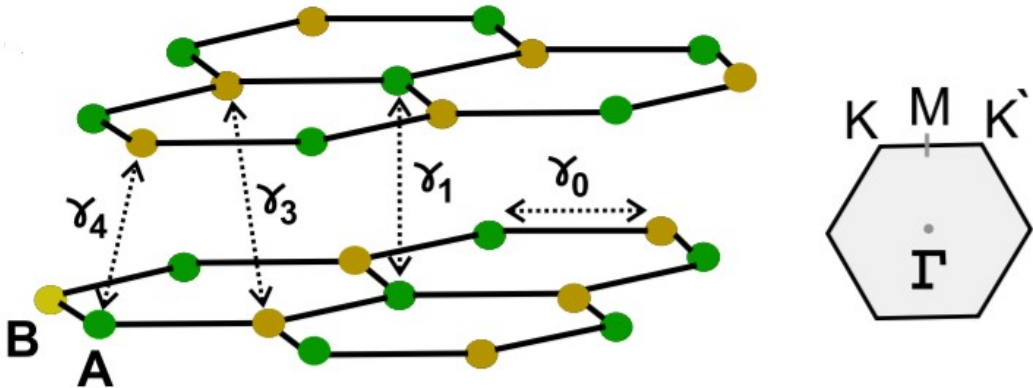


Figure 2.3: Bernal stack bilayer graphene lattice with hopping terms and its Brillouin zone. Left: Two monolayer graphene in AB stacking forming bernal stack bilayer graphene lattice. γ_0 , γ_1 , γ_3 and γ_4 are the hopping terms. Right: Corresponding Brillouin zone that shows high symmetry points. Figure adapted from [28]

Bilayer graphene usually refers to AB stacking or Bernal stacking in which two layers of graphene are stacked on top of each other such that the two layers are shifted by one atomic spacing, as shown in fig. 2.3. The tight binding model gives us the energy dispersion of bilayer graphene. Considering various hopping terms - in-plane nearest neighbour hopping, $\gamma_0 \approx 2.7eV$, hopping between atom A_1 and atom A_2 , $\gamma_1 \approx 0.4$, hopping between atom B_1 and atom B_2 , $\gamma_1 \approx 0.3$ and hopping between atom $A_1(A_2)$ and atom $B_2(B_1)$, the tight-binding Hamiltonian becomes:

$$\begin{aligned}
H = & -\gamma_0 \sum_{\langle i,j \rangle, m, \sigma} (a_{i,m,\sigma}^\dagger b_{j,m,\sigma} + H.c.) - \gamma_1 \sum_{j,\sigma} (a_{j,1,\sigma}^\dagger a_{j,2,\sigma} + H.c.) \\
& - \gamma_3 \sum_{j,\sigma} (b_{j,1,\sigma}^\dagger b_{j,2,\sigma} + H.c.) - \gamma_4 \sum_{j,\sigma} (a_{j,1,\sigma}^\dagger b_{j,2,\sigma} + a_{j,2,\sigma}^\dagger b_{j,1,\sigma} + H.c.)
\end{aligned} \tag{2.8}$$

where $a_{i,m,\sigma}(b_{j,m,\sigma})$ annihilates an electron on sublattice $A(B)$ with spin σ on plane $m = 1, 2$. If we apply a perpendicular electric field to the system, an electrochemical potential Δ is added between the layers. The Hamiltonian in the k space near the $K(K')$ points, ignoring the weaker hopping terms γ_3 and γ_4 , can be represented as [28]:

$$H_{K/K'} = \begin{bmatrix} -\frac{\Delta}{2} & v_F k & 0 & 0 \\ v_F k & -\frac{\Delta}{2} & \gamma_1 & 0 \\ 0 & \gamma_1 & \frac{\Delta}{2} & v_F k \\ 0 & 0 & v_F k & \frac{\Delta}{2} \end{bmatrix} \tag{2.9}$$

The resultant electronic dispersion near the Dirac points is given by:

$$E_\pm^2 = \frac{\Delta^2}{4} + v_F^2 k^2 + \frac{\gamma_1^2}{2} \pm \sqrt{\Delta^2 v_F^2 k^2 + \gamma_1^2 v_F^2 k^2 + \frac{\gamma_1^4}{4}} \tag{2.10}$$

This equation gives rise to four solutions, hence, four bands near the $K(K')$ points, as shown in fig. 2.4. For $\Delta = 0$ and $v_F \ll \gamma_1$, the lowest two bands are given by:

$$E \approx \frac{v_F^2 k^2}{\gamma_1} \tag{2.11}$$

We see that even bilayer graphene does not have a band gap when no external displacement field is applied. But unlike monolayer graphene which has a linear dispersion, bilayer graphene has a parabolic dispersion near the Dirac points, with effective mass $m^* = \frac{\gamma_1}{2v_F^2}$. For $\Delta \neq 0$ and $\Delta \ll \gamma_0$, the lowest two bands are given by:

$$E \approx \frac{\Delta}{2} - \frac{\Delta v_F^2 k^2}{\gamma_1} + \frac{v_F^4 k^4}{\gamma_1^2 \Delta} \tag{2.12}$$

In the presence of a displacement field, we see that a band gap opens up, which can be tuned by changing the applied perpendicular electric field.

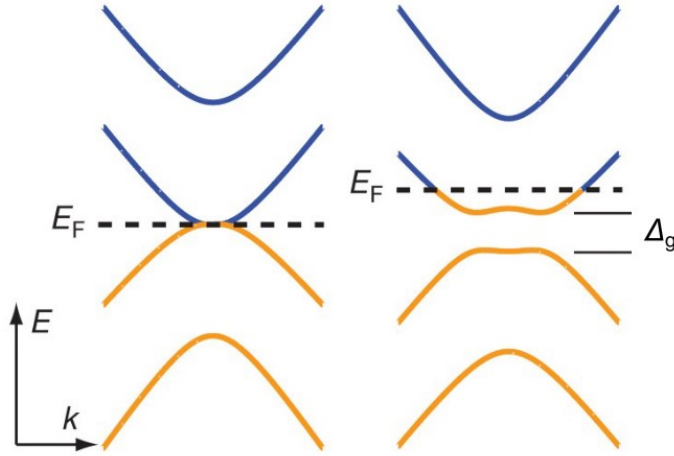


Figure 2.4: Electronic dispersion of bilayer graphene when $\Delta = 0$ (left) and $\Delta \neq 0$ (right). A band gap Δ_g opens up in the presence of an external displacement field. Figure adapted from [29]

2.3 Twisted bilayer graphene

2.3.1 Moiré superlattices

A geometric interference pattern, known as Moiré pattern, is formed when two-dimensional crystals with a lattice mismatch or a relative twist between them are stacked on top of each other. The wavelength of the Moiré pattern in case two layers of graphene is given by:

$$\lambda = \frac{(1 + \delta)a}{\sqrt{2(1 + \delta)(1 - \cos\theta) + \delta^2}} \quad (2.13)$$

where a is the lattice constant of graphene, θ is the twist angle between the two layers and δ is the lattice mismatch between the two layers. Moiré pattern gives rise to effective superlattice potential with a periodicity different from the original lattice. We can see that the Moiré wavelength becomes much larger than the lattice constant for small twist angles. When λ becomes comparable to the Fermi wavelength, the electronic structure

is significantly modified. For example, aligned graphene-hBN heterostructures give rise to secondary Dirac points as a result of the Moiré superlattice potential.

In case of twBLG, the twist between the graphene layers gives rise to formation of a Moiré superlattice and creation of mini Brillouin zone, as shown in fig. 2.5. The mini Brillouin zone can be constructed from the difference between the two $K(K')$ wavevectors for the two layers. Band structure is changed with formation of flat bands with high density of states, which we discuss in the following sections.

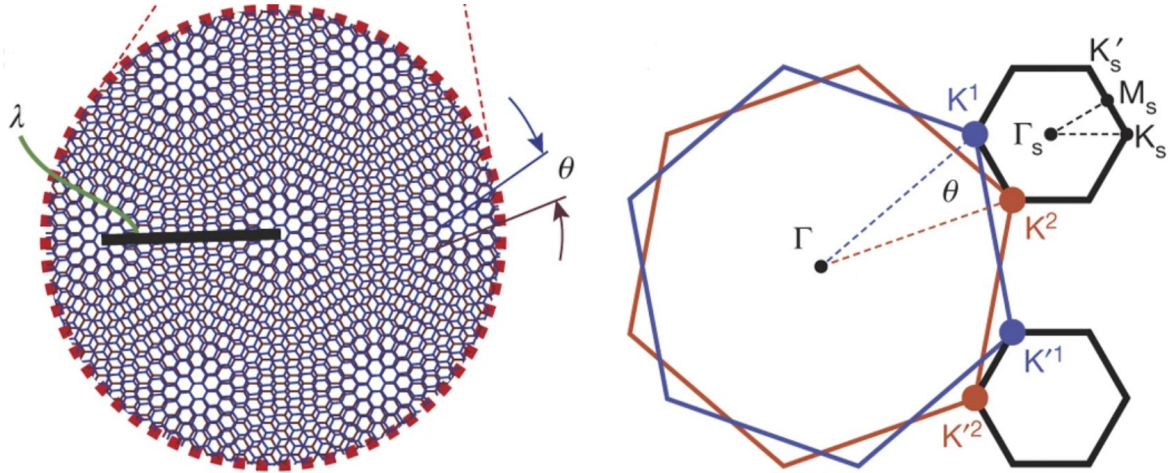


Figure 2.5: twBLG Moiré pattern and its mini Brillouin zone. Left: The Moiré pattern as seen in twBLG. The Moiré wavelength is $\lambda = \frac{a}{2\sin(\theta/2)}$. Right: The mini Brillouin zone is constructed from the difference between the two $K(K')$ wavevectors for the two layers. K_s, K'_s, M_s and Γ_s denote points in the mini Brillouin zone. Figure adapted from [1]

2.3.2 Continuum model developed by MacDonald

The geometry of the bilayer system is characterised by a twist angle θ and a translation vector \mathbf{d} . But commensurability is determined only by the twist angle. We will discuss continuum model developed by MacDonald. [17] In a commensurate structure, sliding one layer with respect to another modifies the unit cell but leaves the bilayer crystalline. So, let's consider AB stacking as the aligned configuration. The positions of the carbon atoms in the two layers are then \mathbf{R} and $\mathbf{R}' = M(\theta)(\mathbf{R} - \tau) + \mathbf{d}$, where τ is a vector connecting the two atoms in the unit cell, and M is a two dimensional rotation matrix within the graphene plane.

The bilayer forms a two-dimensional crystal only at a discrete set of com-

mensurate twist angles. Bloch's theorem doesn't apply microscopically at generic twist angles and hence direct electronic structure calculations are not possible. For twist angles larger than a few degrees, except for a small set of angles that give low-order commensurate structure, the two layers are electronically isolated. As the twist angle reduces, interlayer coupling strengthens and quasiparticle velocity at Dirac point decreases. They derive a low-energy effective Hamiltonian valid for any value of \mathbf{d} and for small twist angles, $\theta < 10^\circ$. [17]

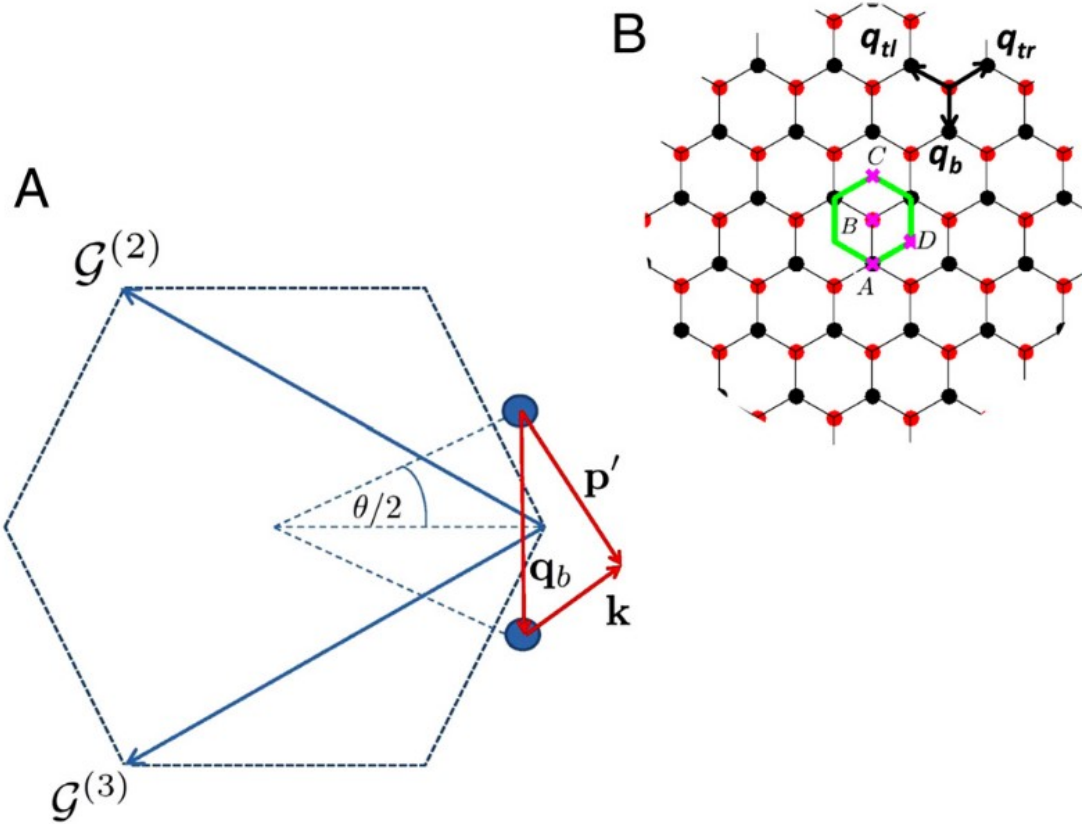


Figure 2.6: twBLG in momentum space (A) Dashed line marks the first Brillouin zone of an unrotated layer. The three equivalent Dirac points are connected by $\mathcal{G}^{(2)}$ and $\mathcal{G}^{(3)}$. The circles represent Dirac points of the rotated graphene layers, separated by $k_\theta = 2k_D \sin(\theta/2)$, where k_D is the magnitude of the Brillouin-zone corner wave vector for a single layer. (B) The three equivalent Dirac points in the first Brillouin zone result in three distinct hopping processes. For all the three processes $|q_j| = k_\theta$. The green solid line marks the Moiré band Wigner–Seitz cell. The red and black circles mark the Dirac points of the two layers. Figure adapted from [17]

The low-energy continuum model Hamiltonian has three terms: two single-layer Dirac-Hamiltonian terms that are associated with the isolated graphene sheets

and a tunneling term that accounts for the hopping between the layers. The Dirac-Hamiltonian for a layer rotated by an angle θ with respect to a fixed coordinate system is given by [28]:

$$h_{\mathbf{k}}(\theta) = -vk \begin{bmatrix} 0 & e^{i(\theta_{\mathbf{k}}-\theta)} \\ e^{-i(\theta_{\mathbf{k}}-\theta)} & 0 \end{bmatrix} \quad (2.14)$$

where \mathbf{k} is the momentum measured from the Dirac point, v is the Dirac velocity, $\theta_{\mathbf{k}}$ is the momentum orientation relative to the x axis. Choosing the coordinate system as shown in fig. 2.6, the decoupled bilayer Hamiltonian is $|1\rangle h(\theta/2) \langle 1| + |2\rangle h(-\theta/2) \langle 2|$, where $\langle i|i\rangle$ projects onto layer i .

Assuming that the interlayer tunneling amplitude between the π -orbitals is a smooth function of spatial separation projected onto the graphene planes, a continuum model is derived. The matrix element,

$$T_{\mathbf{k}\mathbf{p}'}^{\alpha\beta} = \left\langle \Psi_{\mathbf{k}\alpha}^{(1)} \right| H_T \left| \Psi_{\mathbf{p}'\beta}^{(2)} \right\rangle \quad (2.15)$$

of the tunneling Hamiltonian H_T , describes a process in which an electron with momentum $\mathbf{p}' = M\mathbf{p}$ on sublattice β in one layer hops to a momentum \mathbf{k} on sublattice α in the other layer.

In a pi -band tight-binding model the projection of the wavefunctions of the two layers onto a given sublattice are:

$$\left| \psi_{\mathbf{k}\alpha}^{(1)} \right\rangle = \frac{1}{\sqrt{N}} \sum_{\mathbf{R}} e^{i\mathbf{k}(R+\tau_{\alpha})} \left| \mathbf{R} + \tau_{\alpha} \right\rangle \quad (2.16)$$

and

$$\left| \psi_{\mathbf{p}'\beta}^{(2)} \right\rangle = \frac{1}{\sqrt{N}} \sum_{\mathbf{R}'} e^{i\mathbf{p}'(R'+\tau'_{\beta})} \left| \mathbf{R}' + \tau'_{\beta} \right\rangle \quad (2.17)$$

In this case, $\tau_{\alpha} = 0$, $\tau_{\beta} = \tau$, and \mathbf{R} is summed over the triangular Bravais lattice. Using the above equations and the two-center approximation,

$$\langle \mathbf{R} + \tau_\alpha | H_T | \mathbf{R}' + \tau'_\beta \rangle = t(\mathbf{R} + \tau_\alpha - \mathbf{R}' - \tau'_\beta) \quad (2.18)$$

for the interlayer hopping amplitude in which t depends on the difference between the positions of the two carbon atoms. It is found that

$$T_{\mathbf{k}\mathbf{p}'}^{\alpha\beta} = \sum_{\mathbf{G}_1\mathbf{G}_2} \frac{t_{\bar{\mathbf{k}}+\mathbf{G}_1}}{\Omega} e^{i[\mathbf{G}_1\tau_\alpha - \mathbf{G}_2(\tau_\beta - \tau) - \mathbf{G}'_2 \mathbf{d}]} \delta_{\bar{\mathbf{k}}+\mathbf{G}_1, \bar{\mathbf{p}}'+\mathbf{G}'_2} \quad (2.19)$$

where, Ω is the unit cell area, $t_{\mathbf{q}}$ is the Fourier transform of the tunneling amplitude $t(\mathbf{r})$, the vectors \mathbf{G}_1 and \mathbf{G}_2 are summed over reciprocal lattice vectors, and $\mathbf{G}_2' = M\mathbf{G}_2$. Here, momentum is measured relative to the center of the Brillouin zone and not relative to the Dirac point.

The continuum model for H_T is obtained by measuring wave vectors in both layers relative to their Dirac points and assuming that the deviations are small compared to Brillouin-zone dimensions. Although t_q is not precisely known, it should fall to zero very rapidly with q on the reciprocal lattice vector scale. This is because the graphene layer separation exceeds the separation between carbon atoms in a layer by more than twice.

The largest t_q values that enter the tunneling near the Dirac point have $q = k_D$, the Brillouin-zone corner (Dirac) wave vector magnitude, and correspond to the three reciprocal vectors $\mathbf{0}$, $\mathcal{G}^{(2)}$, and $\mathcal{G}^{(3)}$ where the latter two vectors connect a Dirac point with its equivalent first Brillouin-zone counterparts (See fig. 2.6). When only these terms are retained,

$$T^{\alpha\beta}(\mathbf{r}) = w \sum_{j=1}^3 \exp(-i\mathbf{q}_j \cdot \mathbf{r}) T_j^{\alpha\beta} \quad (2.20)$$

where $w = t_{k_D}/\Omega$ is the hopping energy,

$$T_1 = \begin{bmatrix} 1 & 1 \\ 1 & 1 \end{bmatrix}, \quad T_2 = e^{-i\mathcal{G}^{(2)\prime} \cdot \mathbf{d}} \begin{bmatrix} e^{-i\phi} & 1 \\ e^{i\phi} & e^{-i\phi} \end{bmatrix}, \quad T_3 = e^{-i\mathcal{G}^{(3)\prime} \cdot \mathbf{d}} \begin{bmatrix} e^{i\phi} & 1 \\ e^{-i\phi} & e^{i\phi} \end{bmatrix} \quad (2.21)$$

and $\phi = 2/3$. The three \mathbf{q}_j 's are Dirac model momentum transfers that correspond to the three interlayer hopping processes. For $\mathbf{d} = 0$ and a vanishing twist angle, the continuum tunneling matrix is $3w\delta_{\alpha A}\delta_{\beta B}$, independent of position.

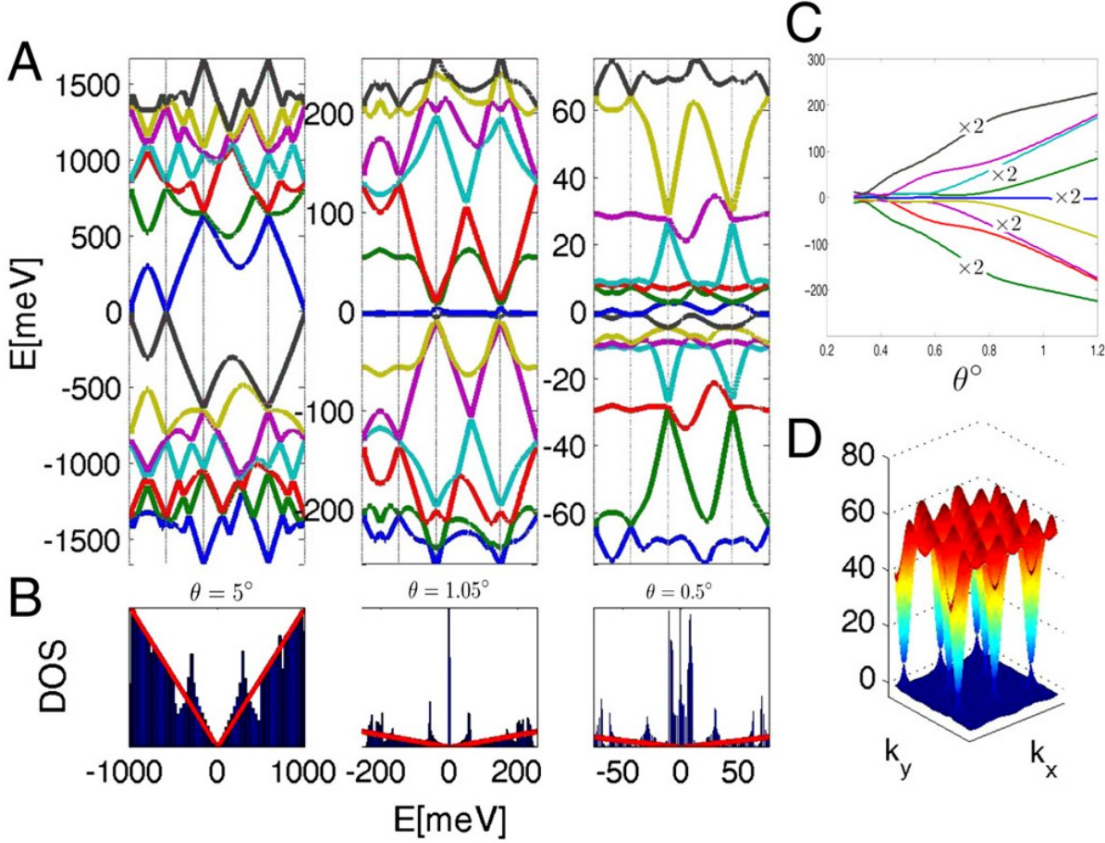


Figure 2.7: Moiré bands (A) Energy dispersion plotted along A-B-C-D-A (see fig. 2.6), for bands closest to the Dirac point. (B) Density of states. (C) Energy as a function of twist angle for the $k = 0$ states. (D) Full dispersion of the flat band at $\theta = 1.05^\circ$. Figure adapted from [17]

In the continuum model, hopping is local and periodic, allowing Bloch's theorem to be applied at any rotation angle irrespective of whether or not the bilayer is crystalline. Solving the Moiré bands numerically using the plane wave expansion illustrated in fig. 2.6, convergence is attained by truncating momentum space at lattice vectors of the order of $w/\hbar v$.

Up to a scale factor, the Moiré bands depend on a single parameter, $\alpha = w/vk_\theta$. Evaluating the Moiré bands as a function of their Brillouin-zone momentum \mathbf{k} for different twist angles gives the result shown in fig. 2.7. For large twist angles, the

low-energy spectrum is virtually identical to that of an isolated graphene sheet, except that the velocity is slightly renormalised. Large interlayer coupling effects appear only near the high energy van Hove singularities discussed in [30].

As the twist angle is reduced, the number of bands in a given energy window increases and the band at the Dirac point narrows. As illustrated in fig. 2.7, it is seen that the Dirac-point velocity vanishes at $\theta \approx 1.05^\circ$, and that the vanishing velocity is accompanied by a very flat Moiré band which contributes a sharp peak to the Dirac-point density-of-states (DOS). At smaller twists, the Dirac-point velocity has a nonmonotonic dependence on twist angle, repeatedly vanishing at the series of magic angles illustrated in fig. 2.8.

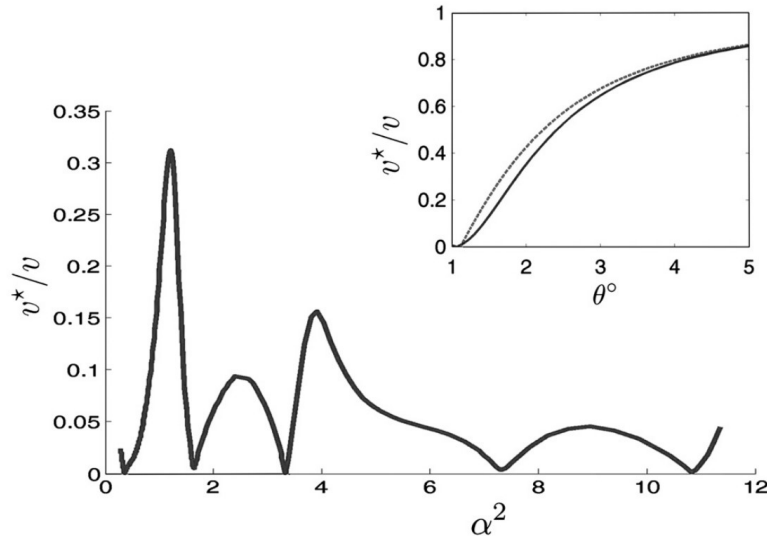


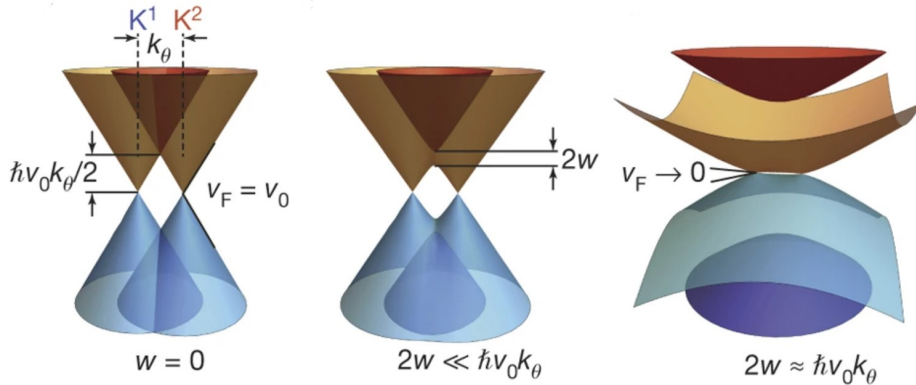
Figure 2.8: Renormalized Dirac-point band velocity. The band velocity of the twBLG at the Dirac point plotted against α^2 , where $\alpha = w/vk_\theta$. Inset shows renormalised velocity at large twist angles. Figure adapted from [17]

2.3.3 Flat bands in twBLG

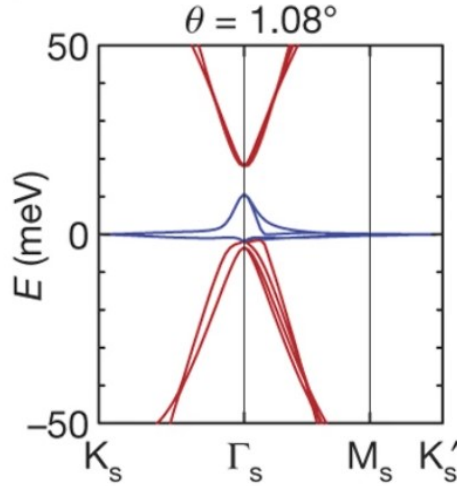
Two graphene layers twisted at an angle with respect to each other gives rise to the formation of a mini Brillouin zone (BZ). The twist angle θ displaces the individual monolayer Dirac points by a wave-vector $|k_\theta| = 2|K|\sin(\theta/2)$, hence forming the mini BZ.

There is hybridisation of the Moiré bands leading to gap openings at the

intersection of the Dirac cones and renormalisation of the Fermi velocity due to the interlayer coupling between the two graaphene layers. A series of magic angles, $\theta = 1.05^\circ, 0.5^\circ, \dots$ have been found at which the Fermi velocity at the Dirac points vanishes that gives rise to flat Moiré bands with large density of states. [17] The flat bands are formed as a result of competition between the interlayer hybridisation energy and the kinetic energy. When the hybridisation energy, $2w$, becomes comparable to the kinetic energy, $\hbar v_F k_\theta$, the lower hybridised states are moved to zero energy leading to bands with very narrow band width (see fig. 2.9). [1]



(a) Illustration of the effect of interlayer hybridization for $w = 0$, $2w \ll \hbar v_0 k_\theta$ and $2w \approx \hbar v_0 k_\theta$, where $v_0 = 10^6 \text{ ms}^{-1}$ is the Fermi velocity of graphene. Figure adapted from [1]



(b) The band energy E of magic-angle ($\theta = 1.08^\circ$) twBLG calculated using tight-binding method. The bands shown in blue are the flat bands. Figure adapted from [1]

Figure 2.9: Electronic band structure of twBLG

2.3.4 Experimental signatures of twBLG

The single-particle picture breaks down due to the presence of flat bands with large density of states near the charge neutrality point, because the Coulomb interactions exceed the kinetic energy in the system. twBLG enters various strongly correlated and topological states when the Fermi energy is tuned within the flat bands. It has been experimentally observed to show correlated insulating states,[1] superconductivity,[2] quantum anomalous Hall effect [4, 31]and ferromagnetism. [5]

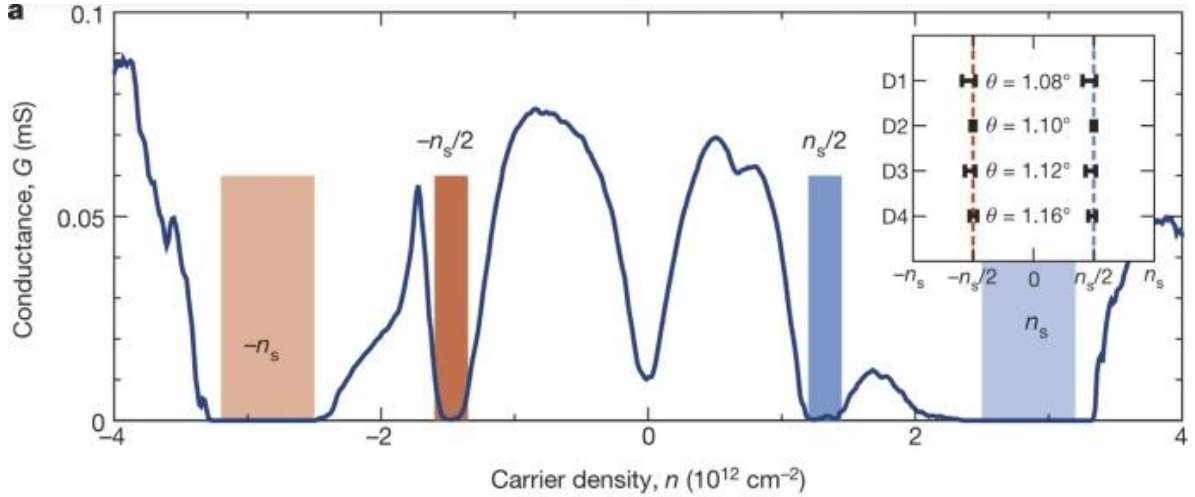
Each Moiré superlattice band is four-fold degenerate at low twist angles. [1]

The charge density required to fill one superlattice band is given by:

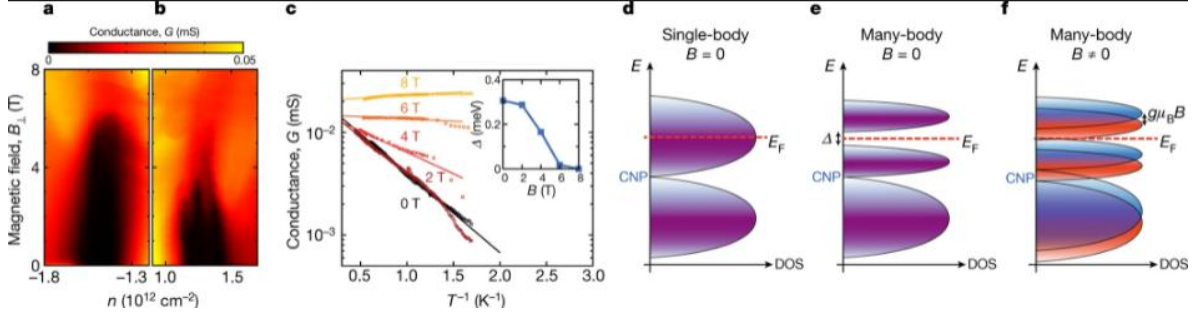
$$n_s = \frac{4}{A} = \frac{8\theta^2}{\sqrt{3}a^2} \quad (2.22)$$

where A is the area of the Moiré unit cell. The filling factor, $v = 4n/n_s$ gives the number of electrons per Moiré unit cell.

Y. Cao and P. Jarillo-Herrero *et al.* demonstrated a flat band nature of twBLG, that is evident from: (1) a reduced Fermi velocity, which is about 1/25 of that in monolayer graphene, and (2) flattening of conductance minimum at the charge neutral point above 40 K. [1] They found a gap opening and an insulating state at half-filling of single-particle Moiré band, with a metal-insulator transition at around 4 K (see fig. 2.10a). The half-filling states at $\pm n_s/2$ are suppressed by the application of a magnetic field (see fig. 2.10b). This effect is seen regardless of the polarisation (parallel and perpendicular). The insensitivity to field orientation suggests that the suppression of the half-filling states is due to a Zeeman effect rather than an orbital effect, because the latter would be affected by only the perpendicular component of the magnetic field. This is indicative of spin singlet state origin.

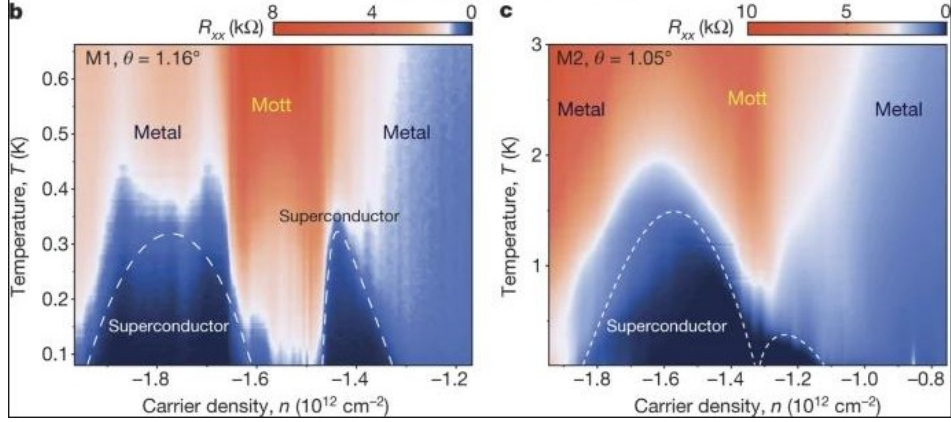


(a) Measured conductance G of magic-angle twBLG device with $\theta = 1.08^\circ$ and $T = 0.3$ K. The inset shows the density locations of half-filling states in the four different devices. Figure adapted from [1]

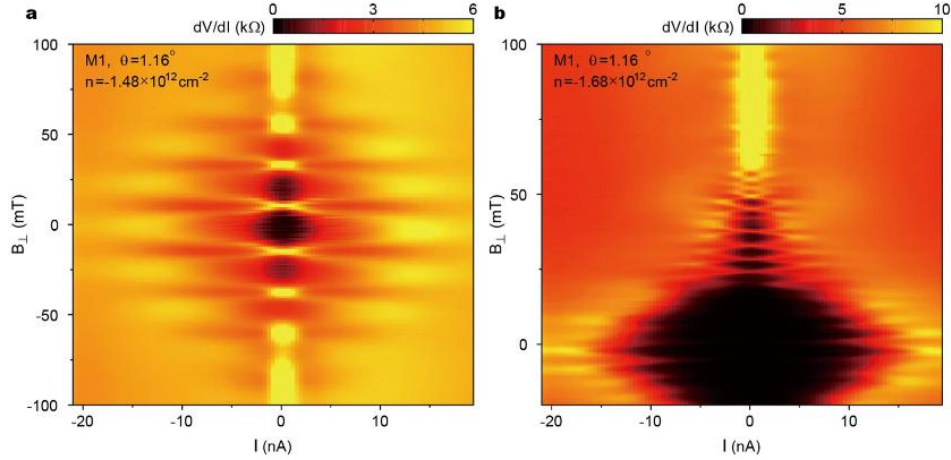


(b) (a,b) Dependence of the conductance on the perpendicular magnetic field of the half-filling states. The measurement is taken at 0.3 K. (c) Arrhenius plot of the conductance of the p-side half-filling state at different magnetic fields. The inset shows the thermal activation gap. (d,e,f) Schematics of the density of states (DOS) in different scenarios, showing gap closing at non zero magnetic field. Figure adapted from [1]

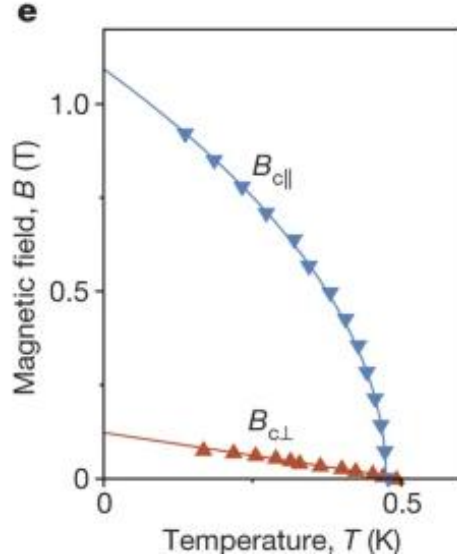
They also found the presence of superconductivity states near the correlated insulating states. This can be seen from the temperature-carrier density phase diagram (fig. 2.11a), which suggests a critical temperature upto 1.7 K. [2] This is similar to phase diagrams with superconductor states flanking Mott states in unconventional superconductors like cuprates. The superconductivity was confirmed by BKT phase transition in voltage-current power law measurements, characteristic of 2D superconductors, and by phase-coherent transport behaviour from SQUID-like interference pattern (see fig 2.11b). The temperature dependence of the perpendicular critical field is consistent with Ginzburg-Landau theory (see fig 2.11c). The zero-temperature parallel critical magnetic field is larger than the value given by BCS theory, suggesting a possible unconventional origin of superconductivity.



(a) Four-probe resistance versus temperature and carrier density for devices with twist angle (b) 1.16° and (b) 1.05° . Two superconducting domes are observed next to the half-filling Mott state. Figure adapted from [2]



(b) Differential resistance dV/dI versus bias current and perpendicular field, at two different charge densities. Periodic oscillations are observed in the critical current. Figure adapted from [2]



(c) Perpendicular and parallel critical magnetic field versus temperature. The fitting curves for perpendicular critical field correspond to Ginzburg–Landau theory for a two-dimensional superconductor. Parallel critical field is fitted to $B_{c\parallel}(0)(1 - T/T_c)^{1/2}$. Figure adapted from [2]

Later, Xiaobo Lu and Dimitri Efetov *et al.* used mechanical squeezing process to improve the angle uniformity, and found resistance peaks at full filling ($v = 4$), quarter ($v = 1$), half ($v = 2$) and three-quarter filling ($v = 3$), i.e., correlated states developed at all integer filling factors, which indicates a full lift of the spin and valley degeneracies. [32] The observed superconductor domes appear not only at a doping close to half filling, but also at around a quarter filling, with a high critical temperature up to 3 K (see fig.2.12).

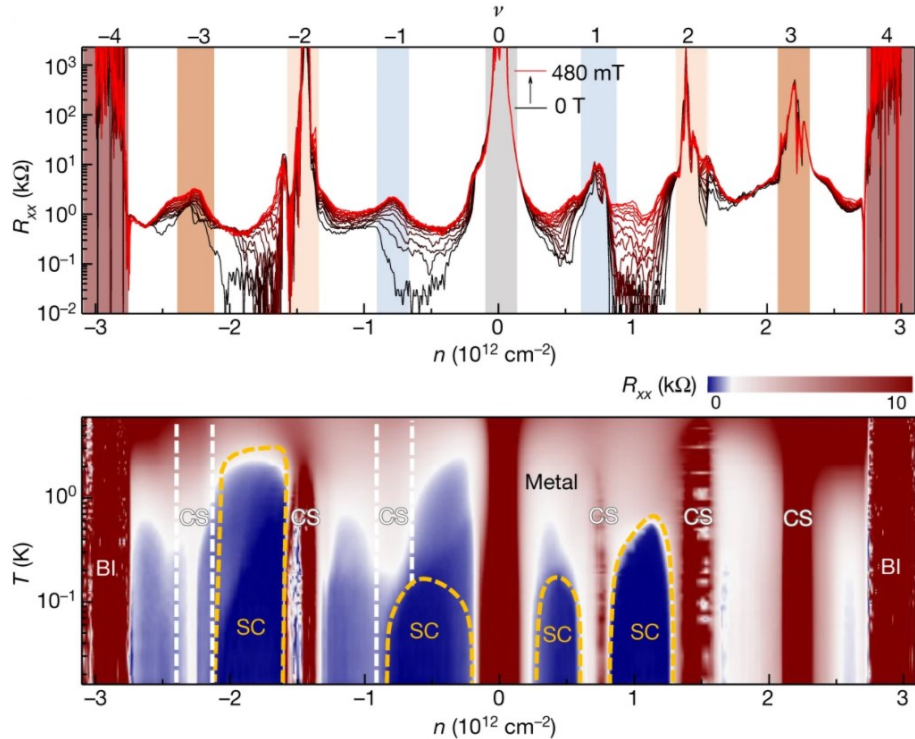


Figure 2.12: twBLG transport signatures. Top: Four-terminal longitudinal resistance plotted against carrier density at different perpendicular magnetic fields from 0 T (black trace) to 480 mT (red trace). Bottom: Colour plot of longitudinal resistance against carrier density and temperature, showing different phases including metal, band insulator (BI), correlated state (CS) and superconducting state (SC). Figure adapted from [32]

The nature of superconductivity in twBLG is still an open question. On one hand, there are a number of similarities between the superconductor state in twBLG and unconventional superconductors: (1) Phase diagram in which superconductor accompanied by Mott insulator, [2, 32] similar to cuprates. (2) Linear-in-temperature resistance observed at higher temperature, [33, 34] similar to strange metal states in unconventional superconductor systems. On the other hand, there are experiments

that suppress correlated insulator states, but keep the superconducting states, hinting at conventional superconductivity in twBLG. One way is by reducing the distance between twBLG and the gate, using thinner hBN dielectric layer, hence decreasing the correlation strength. [35, 36] Another way is by adding a tungsten-diselenide (WSe_2) on top of twBLG, which induces stronger spin-orbit interaction in twBLG, stabilising the superconducting state but closing gaps at all integer filling factors. [37]

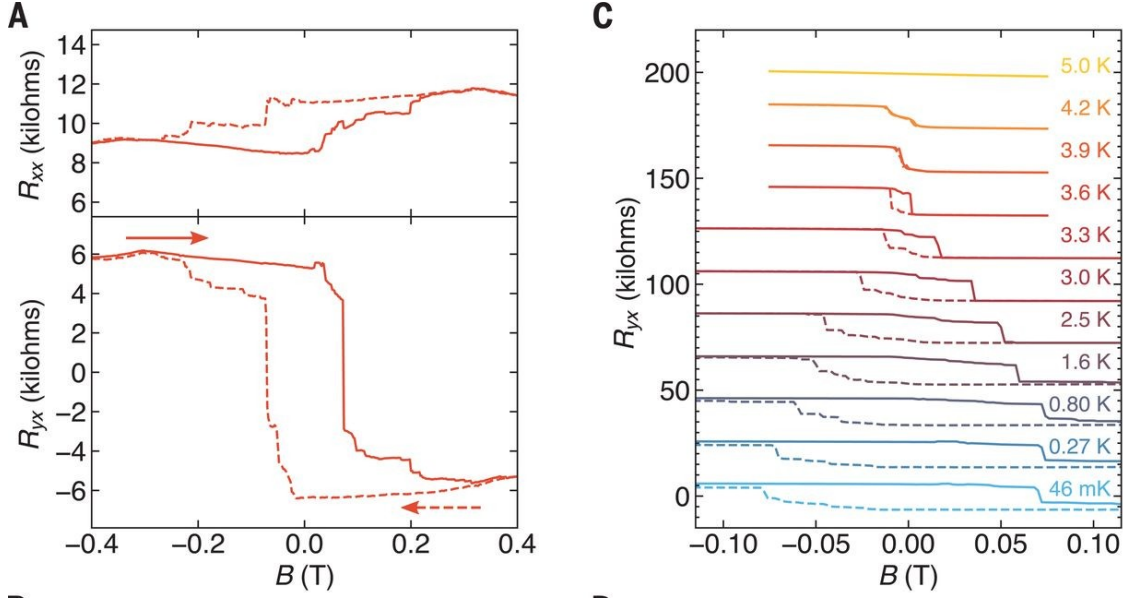


Figure 2.13: (A) Magnetic field dependence of the longitudinal resistance R_{xx} (upper panel) and Hall resistance R_{yx} (lower panel) at 30 mK, showing a hysteretic AH effect resulting from emergent magnetic order. (C) Temperature dependence of R_{yx} versus B between 46 mK and 5.0 K, showing the hysteresis loop closing with increasing temperature. Figure adapted from [5]

Another exciting and surprising discovery is the observation of ferromagnetism and quantum anomalous Hall effect (QAH) in twBLG. An emergent ferromagnetism near three-quarters filling of the conduction Moiré band in twBLG was observed, with a giant zero-field anomalous Hall signal and magneto hysteresis. [5] Later, well-developed quantum anomalous Hall effect with Chern number $C = 1$ was confirmed. [4] Since the twisted bilayer graphene is free of atomic magnetic moment, the counter-intuitive discovery of ferromagnetism [5] and QAH [4] is the result of a correlated Chern insulator. Aligning the bottom graphene layer and the hBN substrate gives rise to strong correlations of the Moiré band and gap opening, leading to the observed effects.

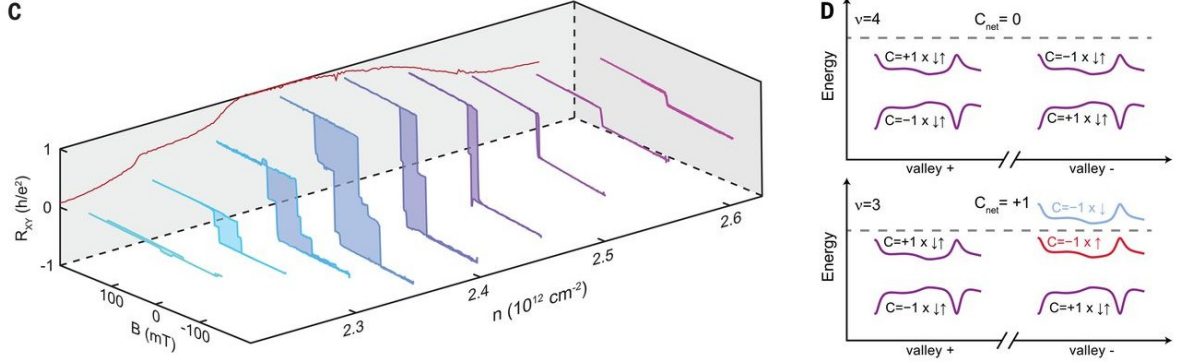


Figure 2.14: (C) R_{xy} as a function of B and n . The rear wall shows field-training symmetrized values of R_{xy} at $B = 0$. Zero-field anomalous Hall signal becomes nonzero when ferromagnetism appears, and it reaches a plateau of h/e^2 . (D) Schematic band structure at filling factors 4 and 3. The net Chern number is 1 at filling factor 3. Figure adapted from [4]

2.4 Tunneling

When the energy bands of two parallel 2D carrier systems are energetically aligned, momentum-conserving tunneling leads to a resonantly enhanced tunneling conductivity and negative differential resistance (NDR). Tutuc *et al.* have worked on tunneling in graphene-insulator-graphene [6] and bilayer graphene-insulator-bilayer graphene. [24, 25, 26] Fig. 2.15 shows the momentum shift caused due to twist between the two graphene layers in the graphene-hBN-graphene device. It also shows the alignment of the bands for different gate voltages. Fig. 2.16 shows the result of this band overlap. There is NDR and resonant tunneling seen. On application of in-plane magnetic field (see fig. 2.17), there is an added momentum that changes band alignment and hence, resonant tunneling conditions.

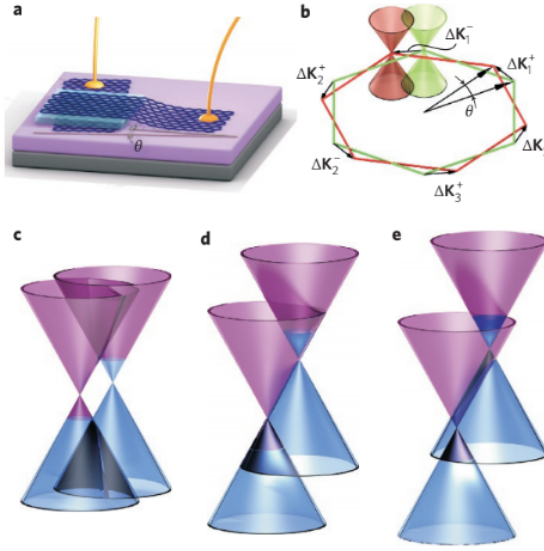


Figure 2.15: (a) Graphene-hBN-graphene device structure. (b) A rotation by θ of the two graphene layers in real space corresponds to the momentum shift K_i^\pm between two Dirac points. (c,e,f) Relative alignment between the top (left cones) and bottom (right cones) graphene Dirac points. The boundary between magenta (empty states) and blue (filled states) marks the Fermi level. Figure adapted from [6]

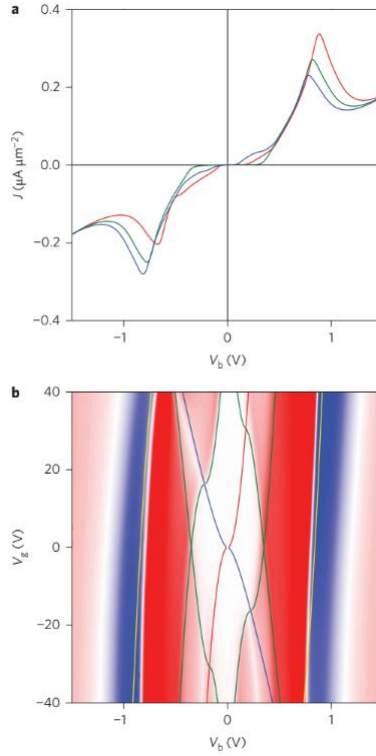


Figure 2.16: (a) Current density vs voltage curves at different gate voltages. (b) Conduction plots as a function of gate and bias voltage. Figure adapted from [6]

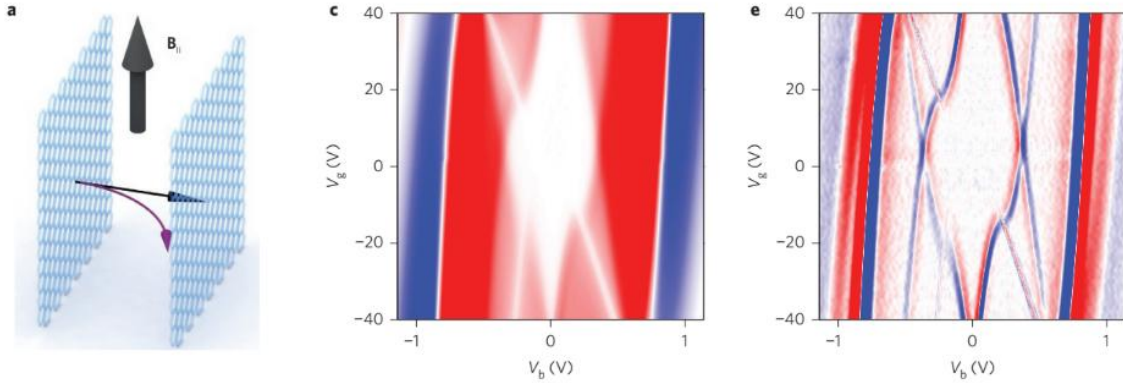


Figure 2.17: (b) Trajectories of the charged quasiparticles tunneling from top to bottom graphene layers in zero and finite magnetic fields caused by the Lorentz force. (c) dI/dV maps measured with a 15 T in-plane magnetic field applied. (e) Difference between the dI/dV maps with and without the in-plane magnetic field. Figure adapted from [6]

Moving on to bilayer graphene-insulator-bilayer graphene, it was seen that NDR still occurs and the tunneling conductivity is exponentially dependent on number of hBN layers (see 2.18). Fig. 2.19 shows that resonant tunneling occurs when charge neutrality points are aligned as it leads to maximum band overlap.

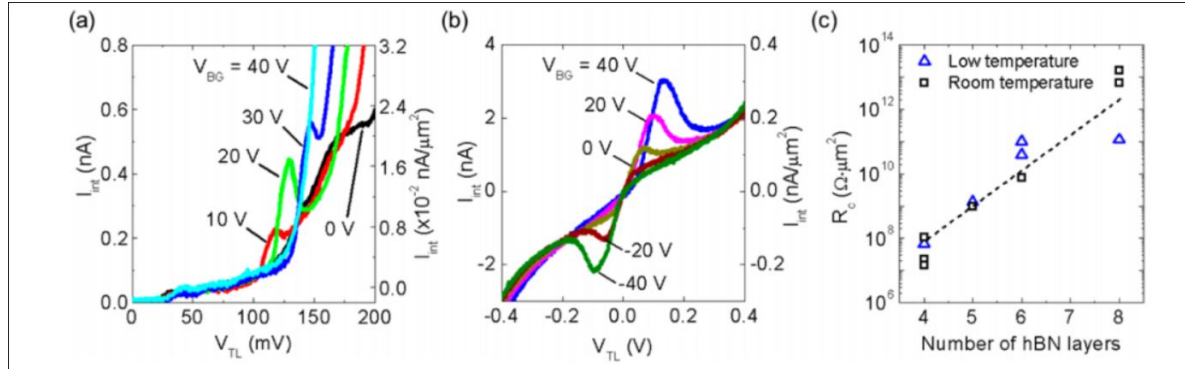


Figure 2.18: Interlayer current-voltage characteristics at (a) 10 K and (b) room temperature in double bilayer graphene - hBN. (c) Normalized interlayer resistance vs number of hBN layers measured in multiple devices and at a low temperature of $T = 1.4\text{-}20$ K and at room temperature. Figure adapted from [24]

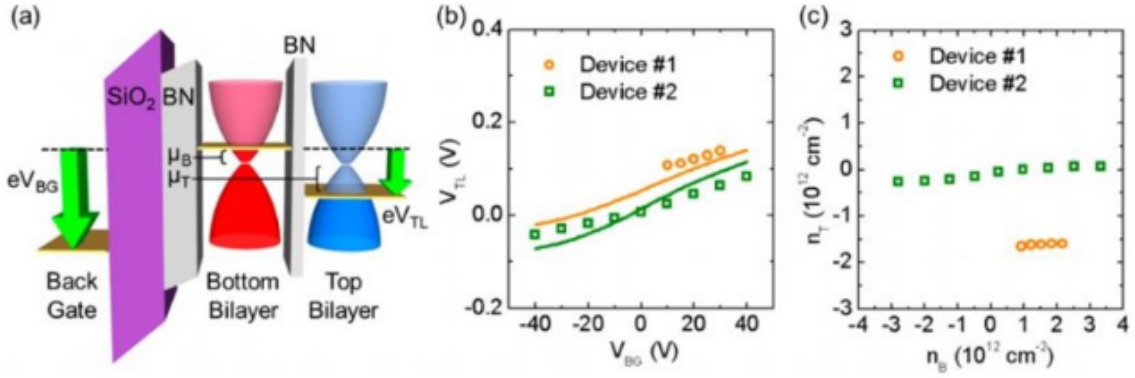


Figure 2.19: Energy band alignment and carrier densities at tunneling resonance in double bilayer graphene - hBN. (a) Energy band diagram of double bilayer graphene when charge neutrality points of top and bottom bilayers are aligned. (b) Interlayer bias vs back gate voltage at tunneling resonance (circles and squares) and when charge neutrality points are aligned (solid line) (c) Carrier densities of top and bottom layer at resonance tunneling. Figure adapted from [24]

Later, it was seen that there are two contributions to tunneling: one is unlike-band tunneling which happens when the overlap happens inside the chemical potential difference, other is like-band tunneling which happens when the bands are completely overlapped. The various possible band alignments are shown in fig. 2.20. Fig. 2.21 shows the same, but for tunneling conductivity. Based on the band alignment one can explain the changes in tunneling current at different gate and bias voltages.

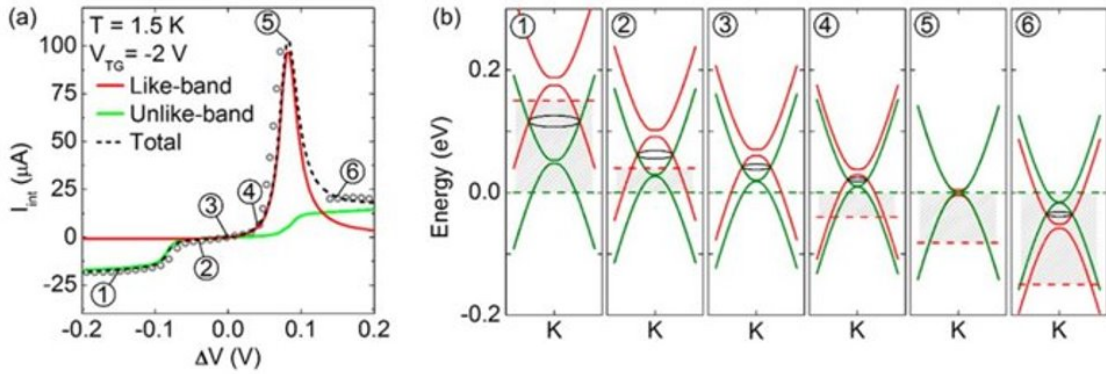


Figure 2.20: Different contributions to the total interlayer tunneling current in double bilayer graphene - WSe_2 . (a) Calculated interlayer tunneling current versus interlayer bias at top gate voltage -2 V and $T = 1.5$ K. The simulated data shows the total interlayer tunneling current (black), along with the like- (red) and unlike-band (green) tunneling. The symbols represent corresponding experimental data. (b) Energy band-alignment of the top (red) and bottom (green) graphene bilayers at various bias voltages. The dashed red (green) line marks the chemical potential of the top (bottom) graphene bilayer. Figure adapted from [25]

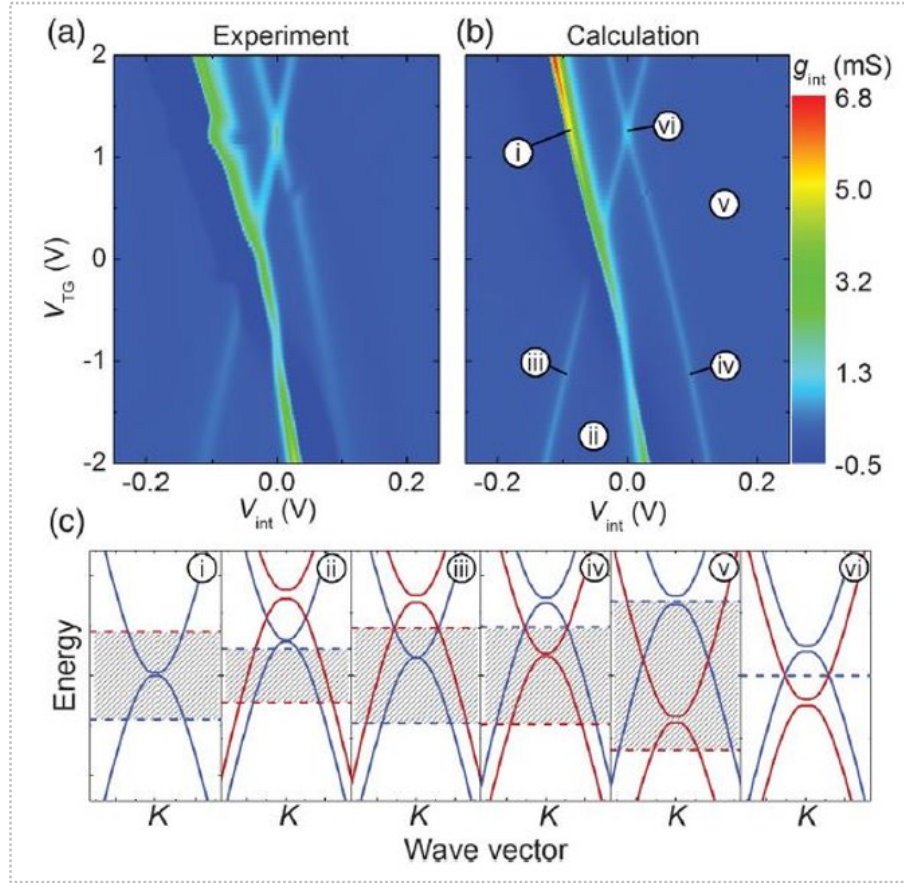


Figure 2.21: Experimental (a) and calculated (b) interlayer conductivity vs interlayer bias and top gate voltage at back gate voltage -20 V and $T = 1.5$ K, in double bilayer graphene - WSe_2 . The points labeled in (b) identify distinct tunneling regimes. (c) Energy band alignment of top (red) and bottom (blue) bilayer graphene bands corresponding to the biasing conditions labeled in (b). The dashed lines mark the two layer Fermi levels. Figure adapted from [26]

Now, looking at graphene-insulator-metal heterostructure, [27] the band diagram of a metal-graphene (MG) junction changes from isolated graphene and metal system at equilibrium, as shown in fig. 2.22. It forms a dipole layer as a result of charge transfer within the equilibrium separation distance. This is similar to having an insulator in between the junction. There is a potential difference ΔV due to the dipole/dielectric and a shift in fermi level of graphene, ΔE . Fig. 2.23 shows various tunneling conditions, along with direction and magnitude of tunneling current. Applying a bias voltage V changes the relative difference between the Fermi levels on each side. If the Fermi level of graphene (metal) is above the fermi level of metal (graphene), tunneling current flows from graphene (metal) to metal (graphene). The magnitude of

the tunneling current depends on the difference between the Fermi levels. In case of twBLG-insulator-metal, estimating the tunneling current isn't straight forward, as the band structure of twBLG is very different from that of graphene. Tunneling measurements are expected to provide insight into the band structure of twBLG, which is rich in electron correlation and has flat bands at magic angle.

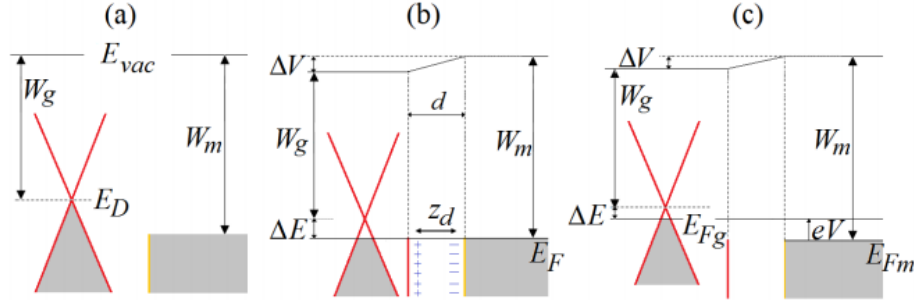


Figure 2.22: (a) Band diagram of an isolated graphene and metal system. (b) Band diagram of a Metal-Graphene (MG) junction at equilibrium showing dipole formation at the interface. (c) Nonequilibrium band diagram of the MG junction. Figure adapted from [27]

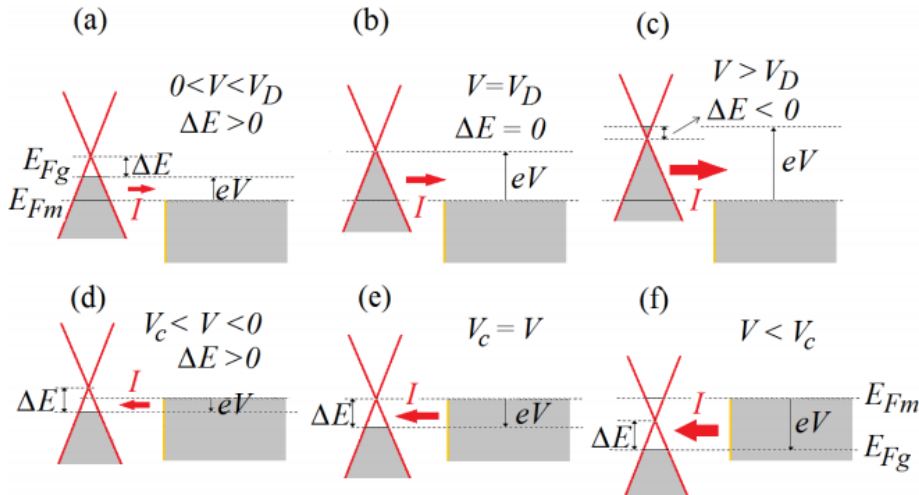
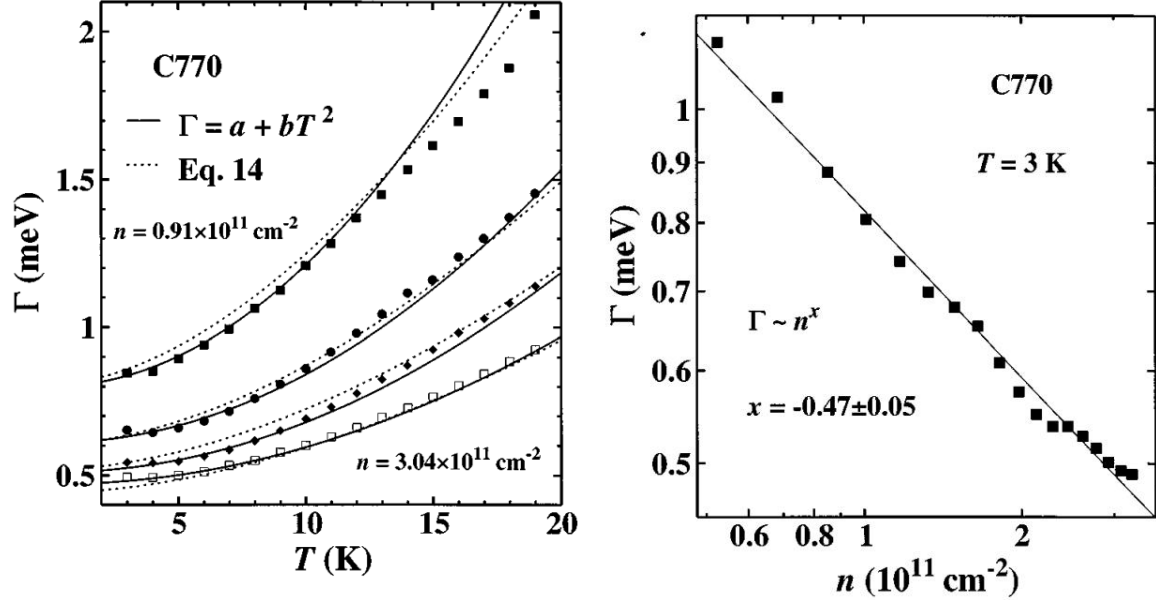


Figure 2.23: Schematic representation of the tunneling current between graphene and metal electrodes. Figure adapted from [27]

As we discussed earlier, in addition to conserving energy E , resonant tunneling between two parallel two-dimensional electron gases (2DEGs) requires the conservation of the in-plane momentum. Tunneling measurements help in the investigation of the broadening of the electronic states within an individual 2DEG, in a way that is not

possible with conventional transport measurements. The lifetime broadening is characterized by the electron spectral function $A(\mathbf{k},E)$, which describes the probability that an electron in a particular \mathbf{k} state has energy E . $A(\mathbf{k},E)$ is strongly peaked near the free-particle energy, with a width determined by the lifetime of the electron.



(a) Temperature dependence of the equilibrium linewidth. The solid lines are fits to the form $a + bT^2$.

(b) Log-log plot of the linewidth versus carrier density at $T = 3$ K.

Figure 2.24: Tunneling measurements done in devices with two GaAs quantum wells separated by a $Al_{0.33}Ga_{0.67}As$ barrier. Figure adapted from [7]

Tunneling measurements done in devices with two modulation-doped GaAs quantum wells separated by a $Al_{0.33}Ga_{0.67}As$ barrier, [7] show the density dependence of the electron-impurity scattering and the temperature dependence of the electron-electron scattering. Fig. 2.24a shows the temperature dependence of the equilibrium linewidth. Only the electron-phonon and electron-electron scattering was expected to show significant temperature dependence. The temperature dependent component of the tunneling linewidth is due to electron-electron scattering as they saw a weak temperature dependence in sheet resistance. This indicates that the mobility is dominated by impurity scattering and the temperature dependent electron-phonon contribution is small. It was observed that the linewidth exhibits an approximate T^2 temperature dependence coming from electron-electron scattering. Fig. 2.24b shows the carrier density

dependence of the equilibrium linewidth. At low temperatures, the electron-electron scattering is negligible, and the tunneling linewidth is due to electron-impurity scattering. They see that the linewidth shows the power-law behavior expected ($\propto n^{-1/2}$) for small-angle scattering from remote ionized impurities.

Coming back to Graphene-hBN-metal heterostructures, signatures of phonon and defect-assisted tunneling have been observed. [8] They observe weak tunneling at low energies which is attributed to the absence of substantial overlap of the metal and graphene Fermi surfaces in momentum space. The enhancement in tunneling at higher energies is associated with the onset of inelastic processes in which phonons in the heterostructure provide the momentum necessary to overcome the Fermi surface mismatch. Fig. shows some of the possible phonon contributions to tunneling considering in-plane momentum conservation. An electron from a pole of the metal Fermi surface can use its out-of-plane momentum and a K-point phonon mode to tunnel on to the graphene Fermi Surface. An M-phonon mode can also contribute to the tunnel current since it can be shifted across the Brillouin zone to the K or K' point. This suggests that several phonons can contribute to tunneling by supplying appropriate out-of-plane momenta to the electrons on the surface of the metal Fermi surface.

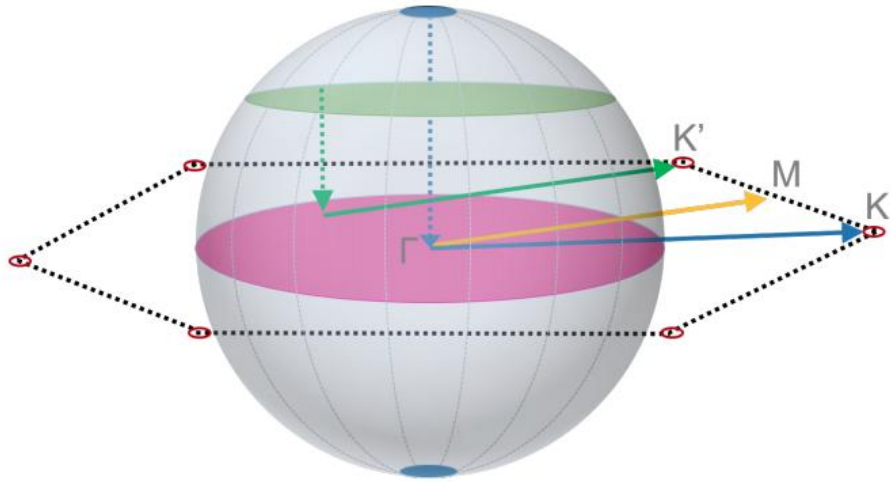


Figure 2.25: Side-view of the Fermi surfaces of graphene and metal showing two possible phonon modes that contribute to tunneling. Figure adapted from [8]

Chapter 3

Methods

In this chapter, we will discuss the experimental techniques that are used to fabricate twisted bilayer graphene devices. The device structure is as shown in fig. 3.1: (1) Top gate is Cr/Au deposition with 5 nm Chromium and 50 nm gold, (2) top hBN is thick hBN around 30 nm, (3) two monolayer graphenes twisted at an angle, (4) tunnel hBN is thin hBN around 2nm, (5) Gold pad with multiple lines is Cr/Au deposition with 5 nm Chromium and 10 nm gold, and (6) $Si - SiO_2$ is Si with an oxide layer on top, around 285 nm. The fabrication of the devices is a very important step as it determines whether we will observe certain features in our measurements. In this experiment, we wish to have a twist angle between the graphene to be close to magic angle, i.e., 1.1° . The thickness of tunnel hBN and the alignment of the flakes are also important in the making of these devices.



Figure 3.1: The device structure that is required in twisted bilayer graphene tunneling experiment.

3.1 Exfoliation of graphene and hBN

There are various ways of preparing graphene flakes. [38, 39] The notable ones are Mechanical Exfoliation and Chemical Vapour Deposition (CVD). CVD can be used to grow large scale continuous graphene sheets in the order of centimetres. But this method doesn't produce graphene flakes that have good electron mobility like mechanical exfoliation. We use Mechanical Exfoliation in our experiments.

In this method, we exfoliate graphene flakes onto $Si - SiO_2$ substrate. We have $Si - SiO_2$ substrate cut into small pieces of approximately $1.5\text{cm} \times 1.5\text{cm}$. We then clean the wafers using sonication, in which the wafers are put in a beaker of acetone and sonicated in either normal or soft mode for 5mins. The wafers are then dipped in IPA and blow dried using N_2 . These steps remove the organic adsorbates from the substrate surface. We worked with three variations of Mechanical Exfoliation:

- Conventional Exfoliation: We place a chunk of natural graphite on a Scotch tape and subsequently cleave it to the fresh regions of the tape, uniformly distributing on the tape. This tape is called the Master Tape. The graphite crystals are then transferred from Master Tape onto a new tape by adhering the second tape to the first and slowly peeling it away. This process is repeated till thin translucent graphite crystals containing tape is made. This step ensures that we have flat regions of graphite on the tape surface. This tape is then stuck on the substrate, and we gently apply pressure using a plastic dropper. We peel off the tape slowly. When the tape is removed, van der Waals force between the substrate and the top layers of the graphite crystals will pull down flakes of graphite ranging from 0.34nm (monolayer graphene) to hundreds of nanometers. Fig. 3.2 shows the conventional exfoliation process.

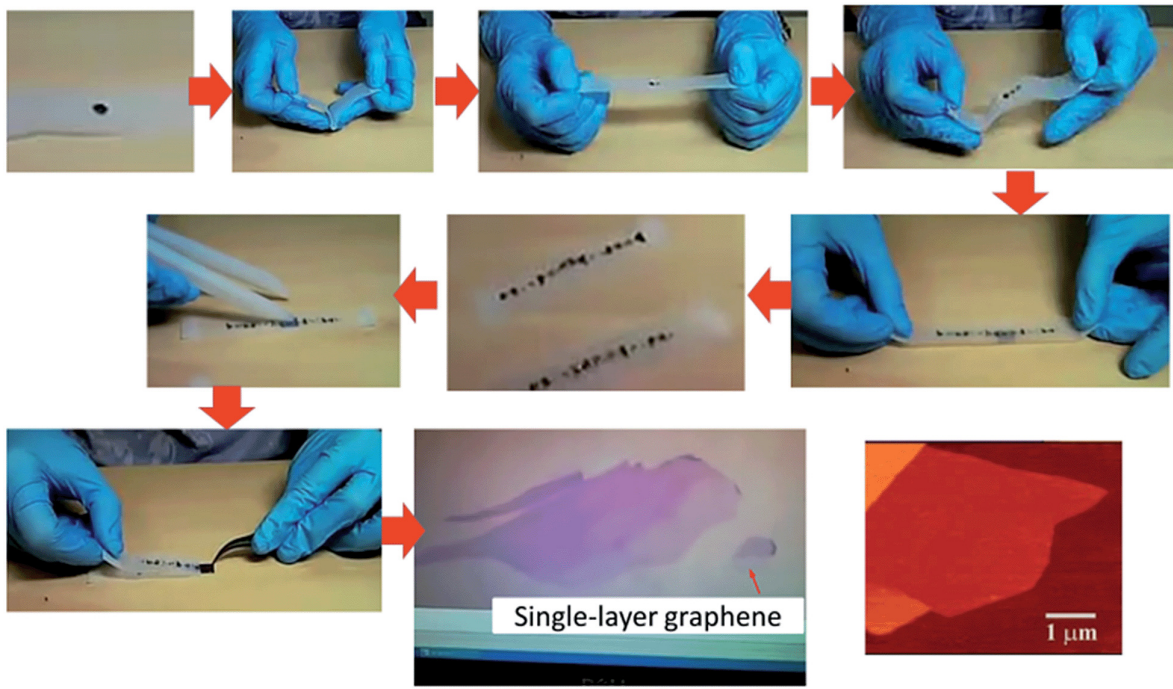


Figure 3.2: Conventional exfoliation process. Figure adapted from [39]

- Hot Exfoliation: We follow the same steps as in conventional exfoliation, with one variation. We heat the substrate using a hot plate at $100^{\circ}C$ for 2-3 mins before sticking the tape onto it. This will improve the adhesion between graphite crystals and the substrate. Fig. 3.3 shows the heater used at lab



Figure 3.3: Heater at lab that has a hot plate used during exfoliation.

- Oxygen Plasma Exfoliation: Here also we follow the same steps as in conventional

exfoliation, with one variation. We clean the substrate using oxygen plasma cleaner before sticking the tape on it. The plasma cleaner setup at the lab consists of: (1) High power expanded plasma cleaner from Harrick Plasma (Model: PDC-002-HP, RF frequency: MHz range, Input power: 200W, Power applied to RF coil: 45 W), (2) Vacuum gauge, (3) Dry vacuum pump, and (4) Oxygen cylinder (see fig. 3.4). This step helps remove adsorbates from the substrate's surface, hence improving the flake transfer, both in number and size, by increasing the adhesion of flakes to the substrate.



(a) Plasma cleaner and vacuum gauge



(b) Dry vacuum pump



(c) Oxygen cylinder

Figure 3.4: Plasma cleaner setup at lab.

We use Hot Exfoliation to get graphene flakes for our devices. The reason we don't use oxygen plasma is that the flakes obtained by this method are hard to pickup using the dry transfer method (section 3.4). We are looking for large monolayer graphene.

We use conventional Mechanical Exfoliation to get hexagonal Boron Nitride (hBN) flakes. The method is similar to that for graphene, with hBN crystals used instead of graphite while making the master tape. We use hBN crystals from Watanabe, K. and Taniguchi, T., NIMS, Japan, known to give good quality thin flakes. [40] We are looking for hBN with two different thicknesses - less than or close to 2 nm (thin hBN) [8] and around 30nm (thick hBN). The thin hBN is used as the tunneling barrier between twBLG and gold pads, while the thick hBN is used as top and bottom hBN next to the gate.

After exfoliation, the substrates with flakes are stored in boxes (fig. 3.5a) and kept in desiccators (fig. 3.5b), which are later subject to flake selection.



(a) A box containing $Si - SiO_2$ substrates with graphene and hBN flakes on them.



(b) A desiccator at lab containing boxes that store empty wafers, substrates with flakes and stacks, tapes and devices.

3.2 Flake selection

3.2.1 Optical microscope

The first thing that is done after the exfoliation of flakes is to check them under optical microscope. The lab has an optical microscope (see fig. 3.6) that has magnifications, 1.25x, 5x, 10x, 50x and 100x.

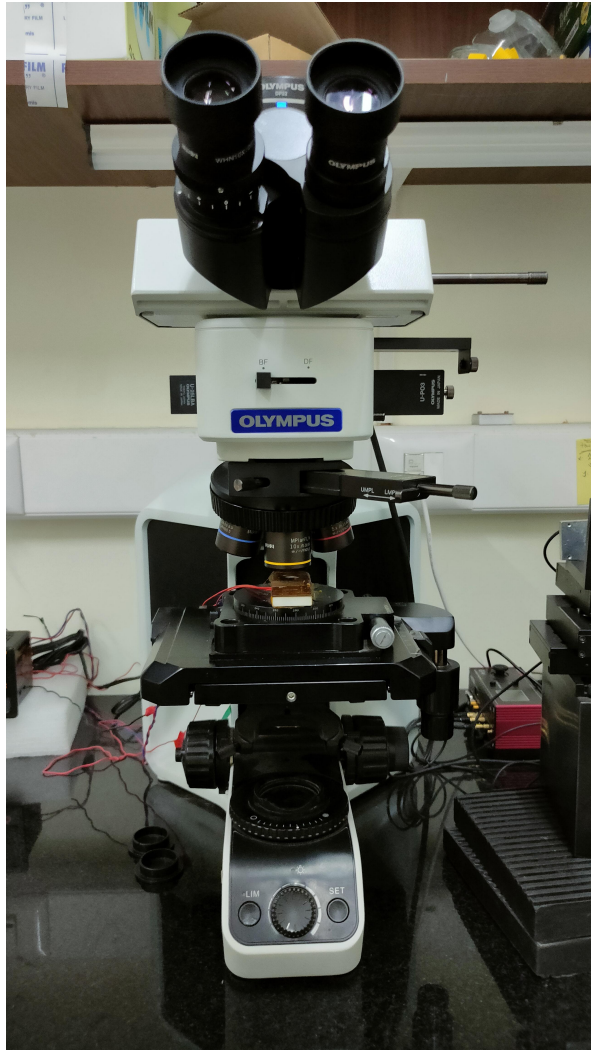


Figure 3.6: Optical microscope at the lab used to find the flakes.

The colour of the flakes under the microscope depends on the thickness of the flake. As the thickness increases, the colour of the flake changes in the following order for both graphene and hBN: less saturated violet, violet, dark violet, dark blue, light blue, green, pink, yellow (see fig. 3.7). Monolayers are similar in colour to tape

residues, are very faint and hard to find. Hence, when checking a substrate for flakes, the magnification is set to 50x. While searching for thin flakes, like monolayer graphene or few-layered hBN, flakes that are close to some reference thick flakes or attached to them are preferred, as they would be easy to handle during transfer. Also, the size of the flakes should be big enough to make stacks and devices. The optical scans of the flakes are saved at varying magnification, which are used to find the flakes during Raman spectroscopy and AFM.

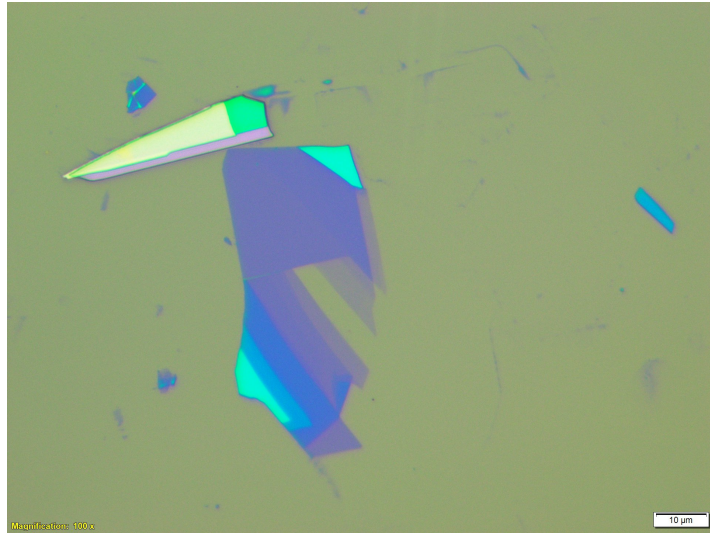


Figure 3.7: hBN flake showing regions with varying thickness.

3.2.2 Raman spectroscopy

Raman spectroscopy is an essential part of graphene research. It is used to determine the number of layers and their orientation. It is also used to probe the effects of perturbations like electric field, magnetic field, strain, disorder, functional groups and doping.

In graphene, the Stokes phonon energy shift caused by laser excitation creates two main peaks in the Raman spectrum: a primary in-plane vibrational mode, G (1580 cm^{-1}), and a second-order overtone of a different in-plane vibration [D (1350 cm^{-1})], 2D (2690 cm^{-1}). [41] D peak is observed only at the sample edge as there aren't significant number of defects in the center of the graphene layers. [42]

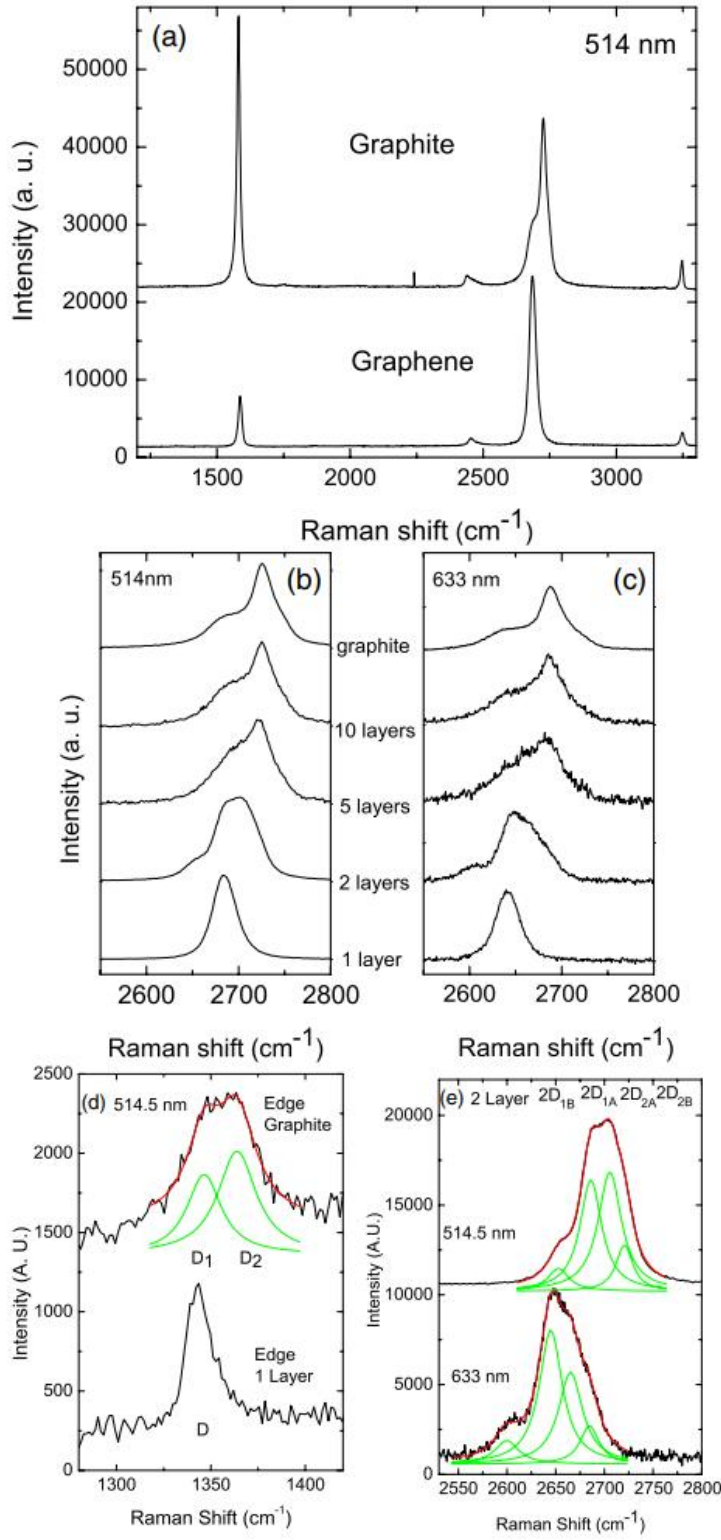


Figure 3.8: (a) Raman spectra of single layer graphene and bulk graphite at 514 nm showing G peak (left) and 2D peak (right). (b,c) Evolution of Raman spectra at 514 nm with number of graphene layers at 514 nm and 633 nm. (d) D band at the edge of single layer graphene and bulk graphite at 514 nm. (e) The four components of the 2D band in 2 layer graphene at 514 and 633 nm. Figure adapted from [42]

On increasing the number of graphene layers, the interaction forces between the AB-stacked graphene lead to a change in the spectrum from that of monolayer graphene. The 2D peak splits into an increasing number of modes that combine to give a wider, shorter and higher frequency peak (see fig. 3.8). Hence, the layer number can be identified from the intensity ratio and the number of peaks needed to fit the 2D peak, for example, bilayer graphene needs four Lorentzian fits arising due to four different phonon-assisted intervalley transitions. [42] In general, for monolayer graphene 2D peak is more intense than G peak, whereas for bilayer, both the peaks show similar intensities. Rotationally disordered (decoupled) multilayer graphene, however, can still have a single intense 2D peak regardless of thickness, [43] though its position and FWHM can depend on the number of layers. [42]

Raman is also used to determine the number of hBN layers in a flake. hBN exhibits a characteristic peak due to the E_{2g} phonon mode and similar to the G peak in graphene. The Raman peak occurs at $\approx 1366\text{cm}^{-1}$, and the peak intensity decreases as the number of layers decreases. [44] For monolayer hBN, peak intensity is about 50 times smaller than for graphene's G peak under the same measurement conditions. The integrated intensity for the hBN peak is proportional to N with high accuracy for the first several layers (see fig. 3.9).

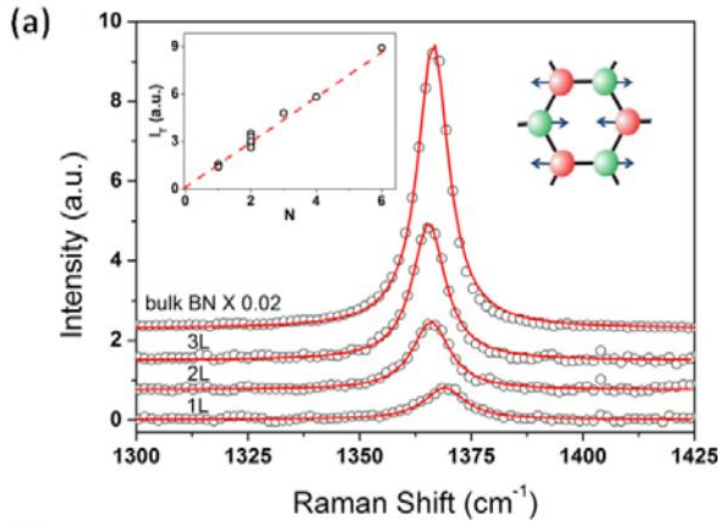


Figure 3.9: Raman spectra of hBN of varying thickness. The left inset show changes in integrated intensity with the number of layers N. The right picture illustrates the phonon mode responsible for the Raman peak. Figure adapted from [44]

3.2.3 Atomic force microscopy

Atomic force microscopy (AFM) is a type of scanning probe microscopy (SPM). It has resolution in the order of fractions of a nanometer, which is useful in mapping the thickness variations in the flakes we use. It is also helpful in determining how clean the flakes are and if they can be used to make stacks. AFM can image almost any type of surface, including polymers, ceramics, composites, glass, and biological samples. This is because, atomic forces are used to map the tip-sample interaction. AFM has a feedback loop using the laser deflection to control the force and tip position. A laser is reflected from the back of a cantilever that includes the AFM tip. As the tip interacts with the surface, the laser position on the photodetector is used in the feedback loop to track the surface for imaging.

Fig. 3.10 shows AFM imaging of hBN flake to determine the thickness, evenness and cleanliness. It can be seen that the thickness of the flake shown is 5nm. From the graph, it is clear that the flake is even in the region selected and it is clean.

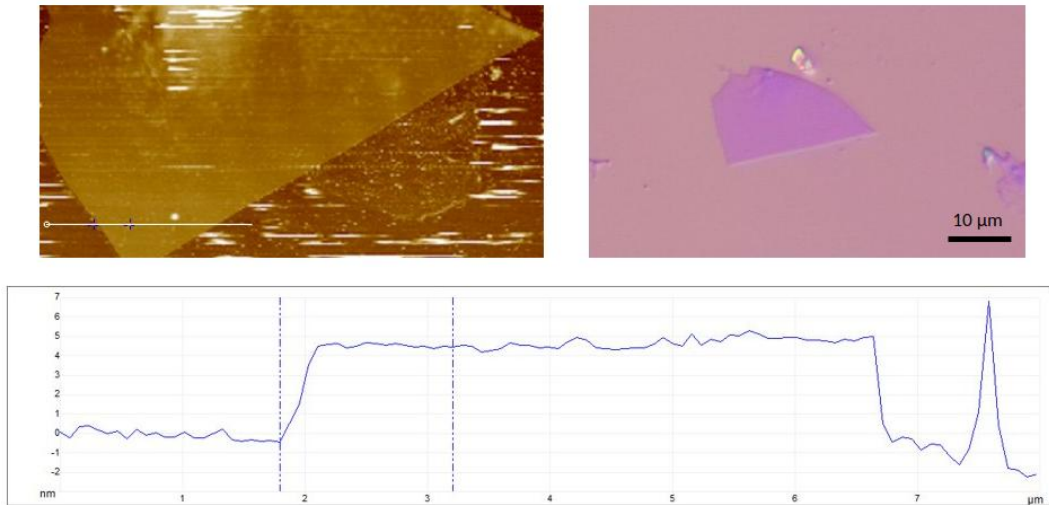


Figure 3.10: AFM of 5nm hBN flake. Top right: Optical image of the flake. Top left: AFM mapping of the flake, to find cleanliness. Bottom: Thickness of hBN flake as a function of position taken along the line shown in the top left figure.

3.3 Stamp creation

Stacks of graphene and hBN are created by putting them on top of each other, using the Pickup and Transfer process. This process involves the use of polymer stamps that can stick to a flake and pick it up. The stamp consists of a coverslip with PPC (Polypropylene carbonate) or PC (Poly(Bisphenol A carbonate)) on hemispherical PDMS (Poly-dimethylsiloxane). The first step is to make the PDMS coverslips. The protocol is as follows:

1. Sonicate coverslips in acetone, wash with IPA and blowdry in N_2 . Fig. 3.12a shows the sonicator used at the lab.
2. Bake the coverslips for 5 minutes at 150 °C to remove moisture.
3. Mix 10 parts PDMS with 1 part curing agent on a clean glass slide using a clean toothpick.
4. Put PDMS onto the coverslips using a toothpick, picking up some PDMS mixture by holding the toothpick vertically.
5. Bake the coverslips at 150 °C for 30 min. A coverslip with PDMS on it looks as shown in fig. 3.11

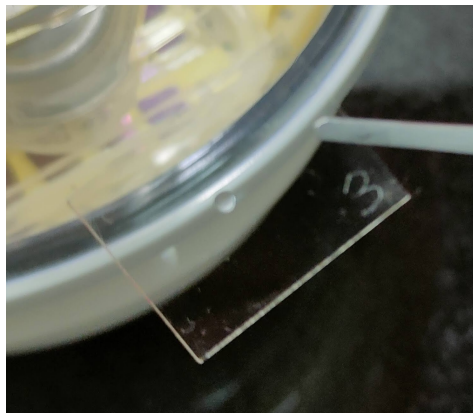


Figure 3.11: A coverslip with PDMS on it.

A layer of PPC or PC is now added on PDMS that is used to pickup the flakes. The steps for this are:

1. Put a drop or two of PPC (15 percent PPC in anisole) or PC (6 percent PC in Chloroform) on PDMS coverslip using a dropper. Use glass dropper for PC.
2. Spin coat it at 3000rpm for 30s by attaching the coverslip to the spin coater with a double-sided tape. Fig. 3.12b shows the spin coater used at lab.
3. Keep the coverslip immediately on the hot plate to bake at 70 °C for 10 mins.



(a) Sonicator (Ultrasound cleaner) at lab



(b) Spin coater at lab

Figure 3.12: Sonicator and spin coater at lab.

PPC or PC solution has to be kept ready before starting stamp making. For making PPC solution:

1. Take a small glass bottle, wash it and heat it at 80 °C for 1hr 30min.
2. Measure and transfer 10ml of anisole in the bottle and add 1.5g of PPC crystals in it, making a solution.
3. Shake the bottle vigorously and leave overnight.

For making PC solution:

1. Wash a small glass bottle.
2. Measure and transfer 3ml of Chloroform in the bottle and add 0.18g of PC crystals in it.

- Leave the bottle overnight.

This coverslip is stuck on the transfer stage using an aluminium plate. This is done with the following steps:

- Keep the coverslip on the metal stick and add EL-9 along the edges of the coverslip using a micropipette.
- Bake this at 90 °C on the hot plate for 2-3 mins.
- Attach the aluminium plate to the stage using double-sided tape.

3.4 Pickup and transfer process

We now discuss the pickup and transfer process, called the dry transfer technique. [18, 45] After the PPC-PDMS and/or PC-PDMS stamp is ready, this process is started in the transfer setup (shown in fig. 3.15). PC-PDMS stamp is used for thin hBN transfer and PC-PDMS stamp for everything else. The choice is based on optimisation. Fig. 3.14 and 3.14 show the schematic of pickup and transfer process used to make a tunnel device, discussed in detail below.

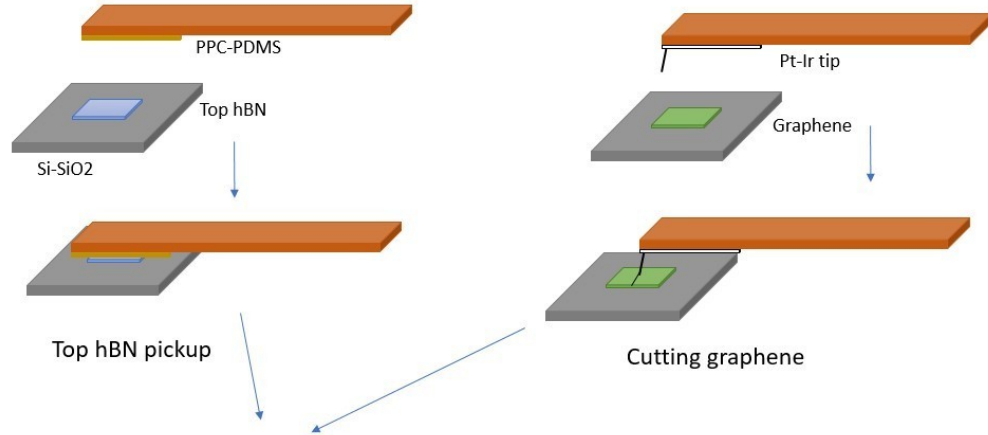


Figure 3.13: Schematic of pickup and transfer process used in making twisted bilayer graphene stack for tunneling measurement: Part 1.

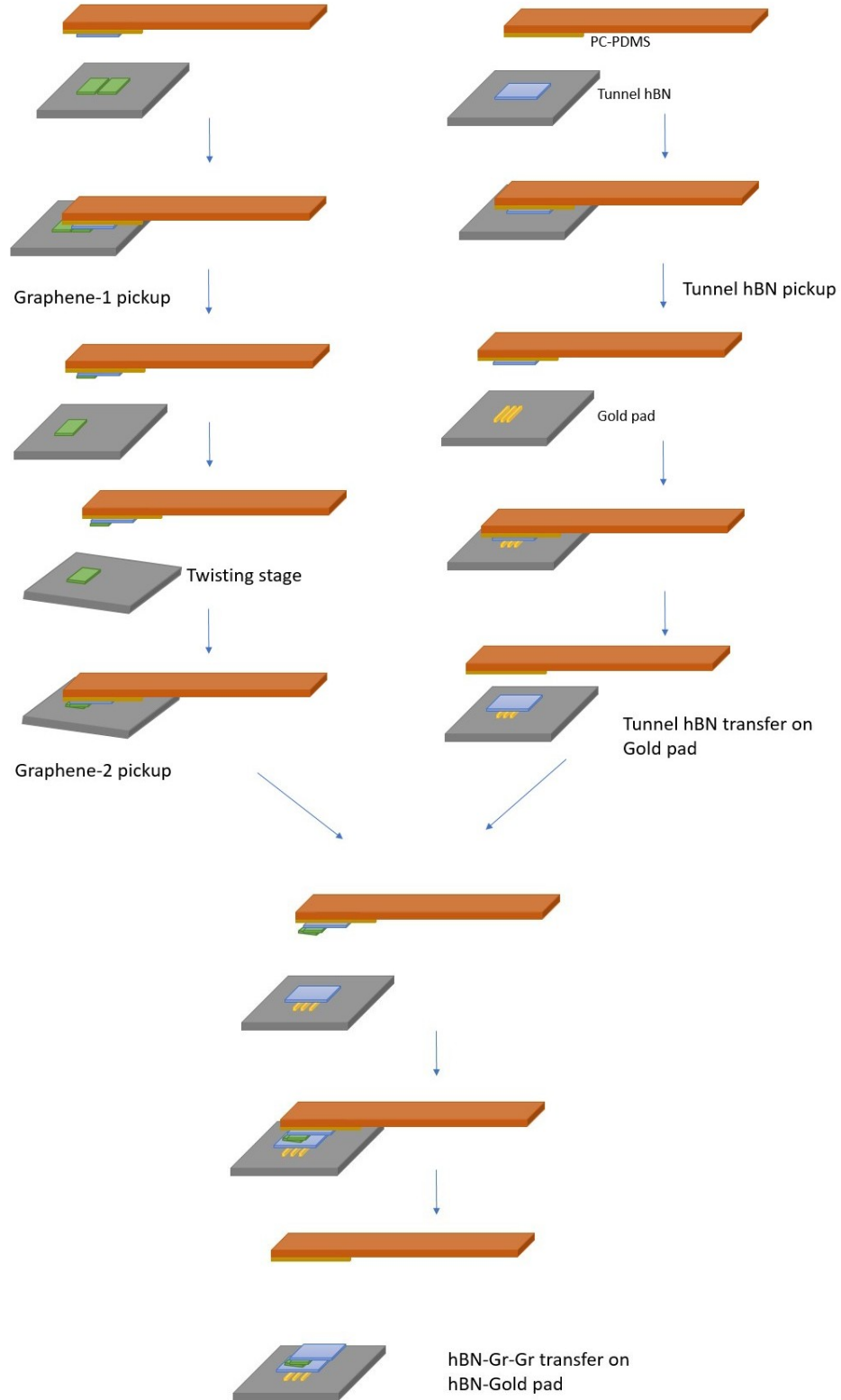


Figure 3.14: Schematic of pickup and transfer process used in making twisted bilayer graphene stack for tunneling measurement: Part 2.

The transfer setup consists of the following parts:

1. OSL2 fiber illuminator: provides illumination for the microscope stage
2. Micro position controller: power source of the rotation stage
3. PID temperature controller: heats the stage
4. Regulated DC power supply: provides voltage to the temperature controller
5. Optical cable: connects illuminator to the microscope
6. Moticam camera: used to see and capture samples under the microscope
7. Optical microscope: has 20x magnification with up to 4x zoom
8. Microscope stage: holds the substrate and has an integrated heater
9. Motorized twist stage: used in twisted bilayer stack making
10. Transfer component: contains an aluminium plate and Piezo actuators
11. Piezo motor controller: powers Piezo actuators

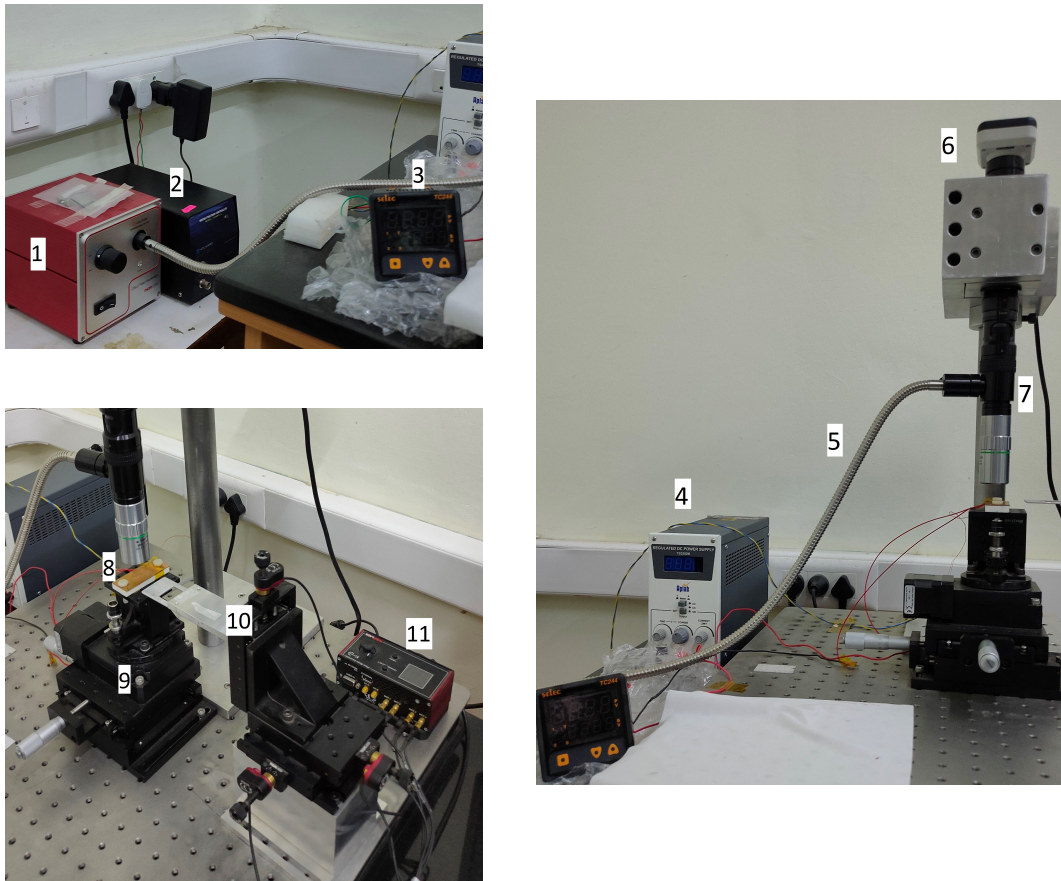


Figure 3.15: Transfer Setup at lab.

The pickup and transfer protocol is as follows:

Part 1: Making a transfer boundary

1. Cover the microscope stage with Kapton tape and put a little square of double-sided tape on top of it.
2. Now, a transfer boundary is made on PDMS. A piece of clean silicon wafer is stuck on the double-sided tape, and the transfer stage aluminium plate is moved between the microscope stage and the objective.
3. Using the Piezo, the coverslip is moved vertically till the PPC-PDMS or PC-PDMS is in focus and center the region with PDMS.
4. The PDMS is moved up and the empty wafer is brought into focus, and the stage heater temperature is set to 63°C for PPC (130°C for PC).

5. The transfer stage is moved down slowly using the Piezo motors while keeping the wafer in focus. When the PDMS touches the wafer, a circle forms on the coverslip. The coverslip is held there for 5 seconds and then moved up. A circular boundary will be seen on the PDMS after this step. This is the transfer boundary where the PDMS will pick up flakes.
6. Finally, remove the wafer and the Kapton tape.

Part 1 can be skipped once we are comfortable with the whole process.

Part 2: Pickup Step

1. Mount the wafer with the hBN/graphene flake to be picked in the same way as before, on the double-sided tape.
2. Follow similar steps as before, except now centre the flake to be picked, directly under the transfer circle of PDMS.
3. Once PDMS touches the wafer, go down till the circle spreads over the flake that needs to be picked.
4. Wait for 10 mins and turn off the heating.
5. Wait till the temperature comes down to around $35^{\circ}C$. Next, move the PDMS up and confirm if the flake got picked.
6. Finally, remove the wafer and the Kapton tape.

Part 3: Transfer Step

Now there are two things that can be done. Either we keep on picking up flakes or transfer the flake/stack onto a clean wafer/gold pad. For the first case, we continue with the steps as above. We will have to take care of alignment during these steps. For the transfer, we perform the following steps:

1. Cover the microscope stage with Kapton tape and put a little square of double-sided tape on top of it.

2. Mount the wafer onto which the flake has to be transferred on the double-sided tape and heat the stage to $75^{\circ}C$ for PPC ($180^{\circ}C$ for PC)
3. Touch the PDMS with the flake over the area to be transferred on and wait for 10 min.
4. Move the PDMS up and check if the flake got transferred.
5. Remove the wafer and the Kapton tape.
6. Remove the coverslip from the aluminium plate by dissolving EL-9 using acetone.
7. Finally, clean the coverslip and the wafer. They are kept in anisole overnight (Chloroform for 2 hours) to dissolve the PPC (PC). Wash them with IPA (IPA and acetone), and blowdry with N_2 .

Fig. 3.16 shows the pickup of thin hBN and transfer onto the gold pad, which is a part of twisted bilayer graphene stack making. (See section 3.5)

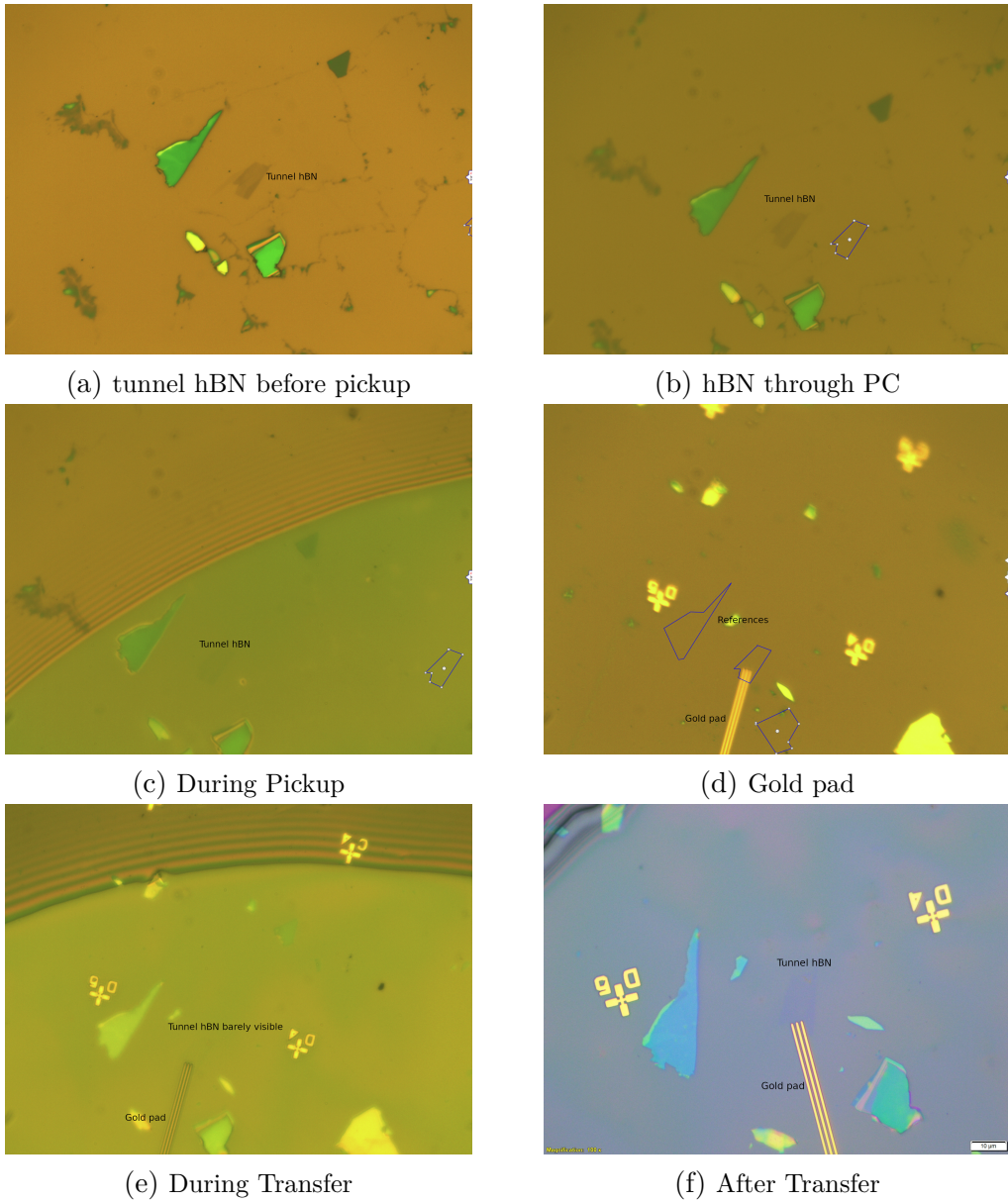


Figure 3.16: Pickup and Transfer of thin hBN on gold pad (bottom tunneling electrode).

3.5 Twisted bilayer graphene stack

hBN-graphene-graphene-hBN-gold pad stacks are required to be made for our devices. Here the top hBN encapsulates the twisted bilayer graphene. The two graphene flakes are aligned at magic angle of 1.1° . The hBN on the gold pad acts as a tunneling barrier. The whole process consists of two parts. One is to transfer thin hBN onto the gold pad, and the other is to make a hBN-graphene-graphene stack on PPC. We follow the protocols as mentioned in section 3.4, with one extra step during the stack preparation.

The graphene is cut in half using a Pt-Ir tip (see fig. 3.17), and one half of the flake is picked up with hBN, the stage is twisted by $\approx 1.2 - 1.4^\circ$ (the twist angle changes to $\approx 1.1^\circ$ due to relaxation) and the other half of the flake is picked up with graphene.

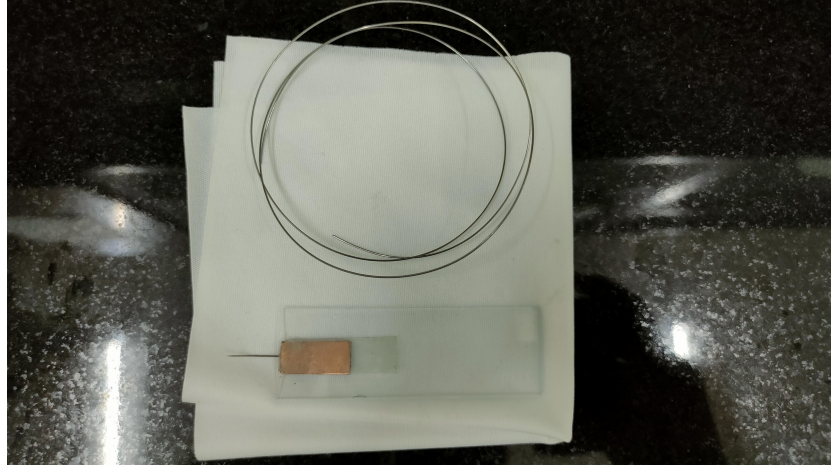
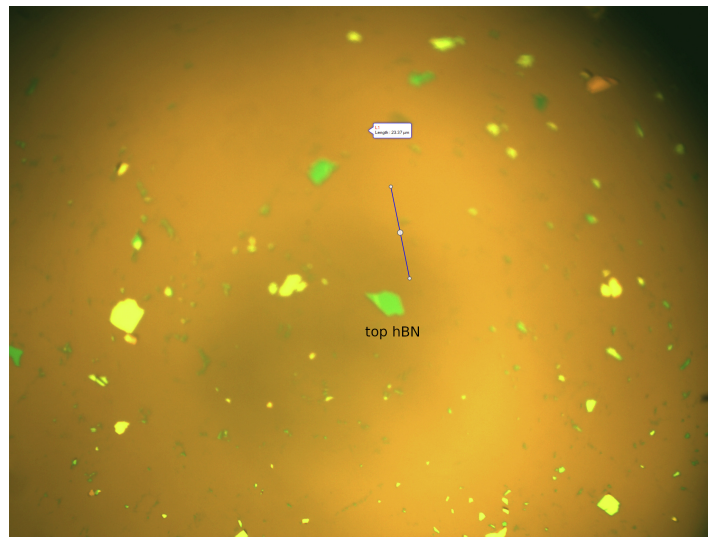


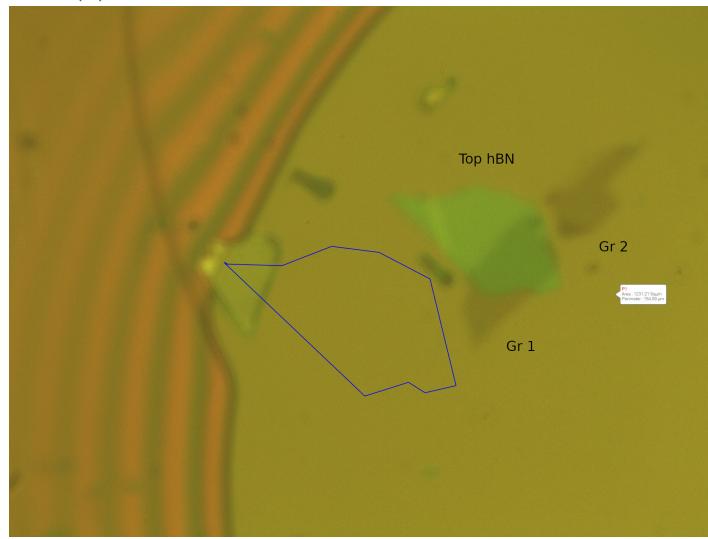
Figure 3.17: Pt-Ir tip that is used in cutting graphene flake and Pt-Ir wire.

The hBN-gold pad substrate is first annealed, which helps in removing residues present on the flake, making it better for using it in our device. Then the hBN-graphene-graphene stack is transferred onto the hBN-gold pad substrate, giving us the final stack. This process is called the cut and stack method. [36] If the graphene is torn in half by hBN and picked up followed by picking the other half by graphene, instead of cutting the graphene with a tip, the process is called the tear and stack method. [18, 21] Cut and stack method is preferred over tear and stack in our experiment. This is because in tear and stack, since the graphene flake is torn by hBN, it creates wrinkles and strain in the other half of the flake that is left. This will lead to an uneven angle when twisted bilayer is made, giving a bad sample.

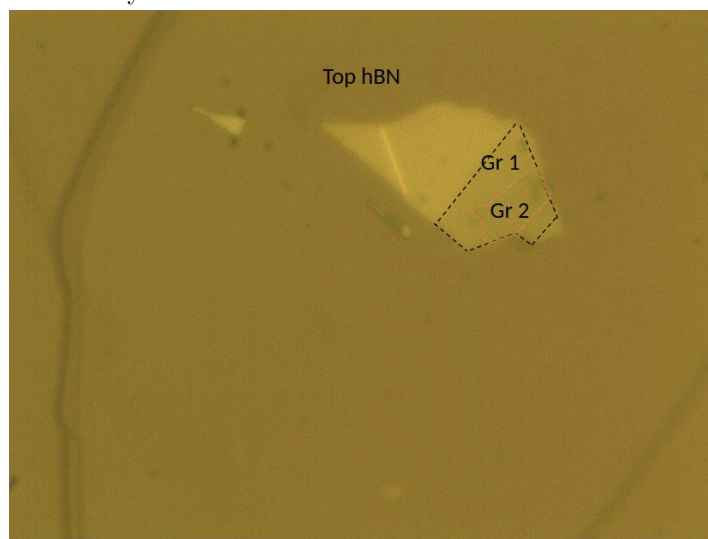
Fig. 3.18 shows the making of the hBN-graphene-graphene stack, which is a part of twisted bilayer graphene stack making. After stack making, there are several steps before we have sample ready for measurement: e-beam lithography, dry etching and gold deposition, which were done by Radhika.



(a) hBN flake before pickup that acts as top hBN



(b) hBN flake picking up one half of the graphene flake that has already been cut



(c) hBN-graphene picking up the other half of the graphene flake

Figure 3.18: Making hBN-graphene-graphene stack on PPC.

Chapter 4

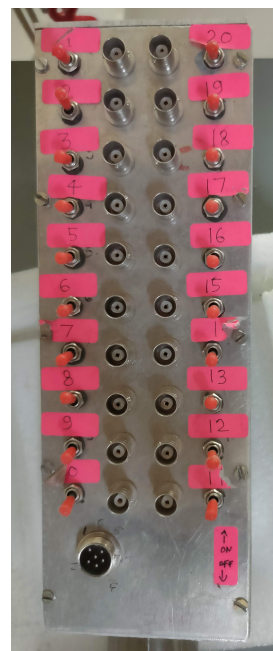
Measurements

4.1 Sample insertion and instruments used

After fabrication, the sample is attached to the chip carrier (see fig. 4.1a). The chip carrier is then mounted onto a header connected to the top of the dip stick (see fig. 4.1b), and covered with dipper jacket. This is then dipped in either liquid N_2 , and the instruments are connected for measurement. Low temperature and magnetic field measurements are done using cryogen-free dilution refrigerator at the lab.



(a) Chip carrier



(b) Top of the dip stick

Figure 4.1: Sample insertion.

The various instruments at the lab that are used in our experiments are shown in fig. 4.2.



(a) Digital multimeter



(b) Current amplifier



(c) Sourcemeter



(d) Lock-in amplifier



(e) Kepco DC voltage source

Figure 4.2: Instruments used at lab.

4.2 Checking contacts

The first step in any measurement is to check the contacts of the sample to make sure that everything is ok. There are possibilities of the contacts shorting, which will affect the measurement. The circuit for checking contacts is shown in fig. 4.3. The lock-in amplifier (LIA) provides AC voltage and is set to 1 V. The configuration is: sensitivity = $200 \mu\text{V}$, low noise, time = 300ms, 24dB. It is connected to a voltage divider that has resistances, as shown in fig. 4.3: $R_1 = 100 \text{ k}\Omega$ and $R_2 = 10 \Omega$. This reduces the voltage coming out by a factor of $R_2/(R_1 + R_2) \approx 10^{-4}$. In our case, the output voltage is $100 \mu\text{V}$. This voltage is sent to a resistor, which is either $5 \text{ k}\Omega$ or $10 \text{ M}\Omega$ based on

the contact that needs to be checked. The resistor chosen has approximately the same resistance as the sample. twBLG contacts give resistance in $k\Omega$ range, while tunnel contacts give resistance in the order of $M\Omega$. The resistor is connected to the contact in the sample. All the other contacts in the sample are grounded. The voltage drop across the resistor is measured by connecting A and B to LIA input.

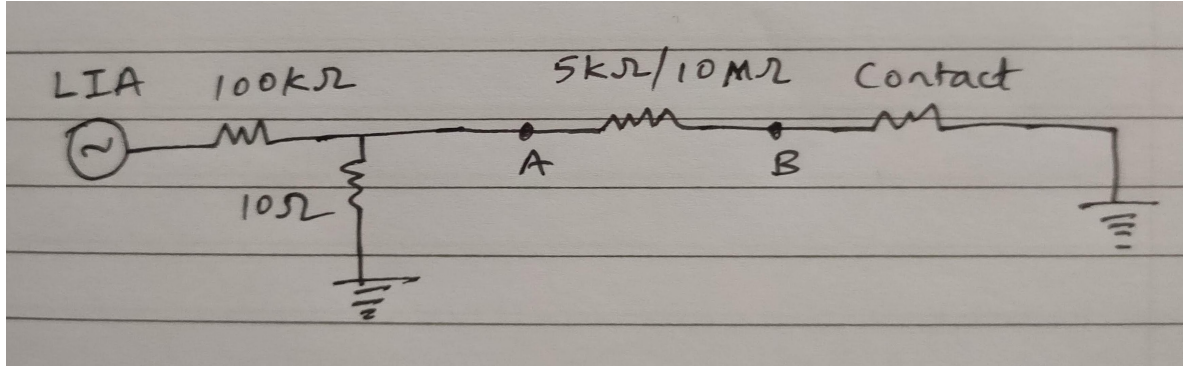


Figure 4.3: Circuit diagram for checking contacts in the sample. LIA is Lock-in amplifier that provides an AC signal of 1 V and 13 Hz. It is connected to a voltage divider, followed by a resistor which is connected to the contact that needs to be checked (other contacts are grounded). Points A and B are connected to LIA input to measure the voltage across the resistor.

The protocol to check the contacts is as follows:

- Ground all the contacts in the sample and switch on LIA.
- Measure and note the voltage drop across the resistor using LIA - V_1
- Set LIA to zero and open the contact that needs to be checked, keeping all others grounded.
- Turn on LIA. Measure and note the voltage drop across the resistor using LIA - V_2
- If $V_2 \approx V_1/2$ the contact is good for twBLG contact. If $V_2 \approx 2V_1/3$ the contact is good for tunneling contact.

The conditions mentioned above come from considering contact resistance to be equal to the resistance of the resistor. In the case of $5 k\Omega$, on opening contact, the voltage drops by half as now the voltage will divide equally between the resistor and the

contact. In the case of $10 \text{ M}\Omega$, on opening the contact, we need to consider the resistance coming from the LIA input, which is $10 \text{ M}\Omega$. Due to this, the effective resistance between point B and ground becomes $5 \text{ M}\Omega$. So the voltage drops to $10/(10+5)$ of the original value.

4.3 Checking gate leakage

Gate leakage check is also an important step before doing measurements. This step checks if the gates are good and not shorting with the stack and leading to gate leakage. The protocol for checking gate leakage is as follows:

- Close all the contacts and connect a gate contact to the sourcemeter. The compliance is set based on the device measured.
- Slowly increase the voltage in steps of 0.1 V and observe the current reading. If the current shows overload for low voltages, then the gate is leaking. Repeat the same for negative voltages. The leakage depends on the compliance set based on the device.

If no leakage is seen, we set the limits till which we sweep the gates based on the value of the voltage at which current shows overload.

4.4 Transport measurement

Transport measurements are usually the first set of measurements done on a sample to characterise its electronic properties. We have done four-probe measurement in our experiment. 4 probe measurement is better than two-probe, as it eliminates the contact resistances. The circuit for performing four-probe transport measurement is shown in fig. 4.4. The lock-in amplifier (LIA) provides AC voltage and is set to 1 V . The configuration is: frequency = 13 Hz , low noise, time constant = 300ms . It is connected to a $100 \text{ M}\Omega$ resistor, which helps in finding the resistance across the contacts (explained later).

The current is sent to the sample through the source, and the drain is grounded. One of the gates is connected to a sourcemeter for sweeping, while the other gate is set to a constant value using another sourcemeter. The voltage drop across the contacts (V_{AB}) is measured using LIA. We can do both normal transport and hall measurements with this method. If the two contacts chosen are on the same side of the sample, then it is normal transport measurement (R_{XX}), and if the two contacts chosen are on the opposite sides of the sample, then it is hall measurement (R_{XY}).

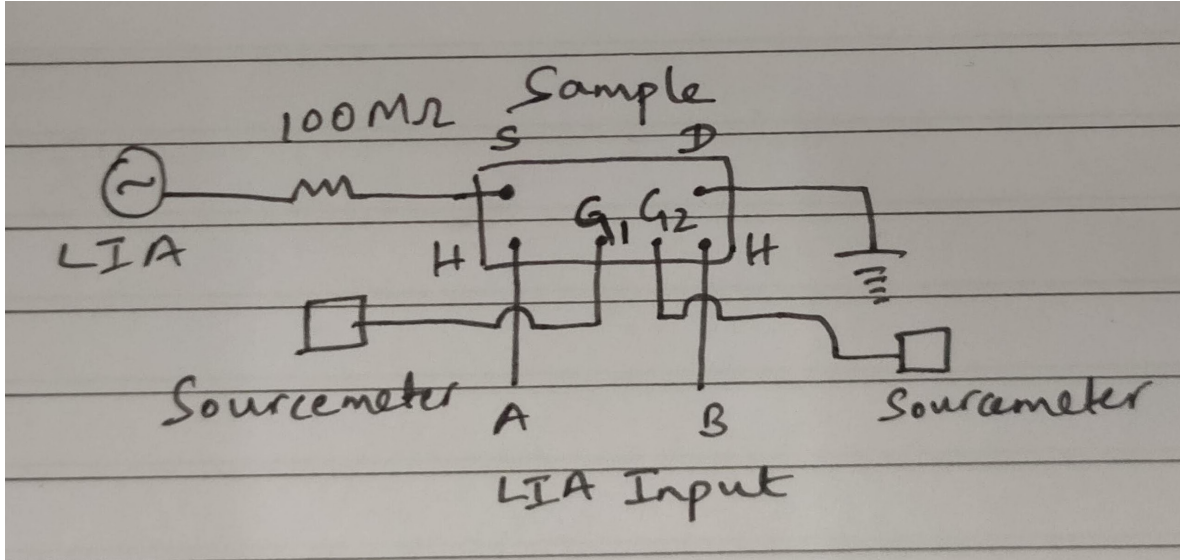


Figure 4.4: Circuit diagram for transport measurements in the sample. LIA is Lock-in amplifier that provides AC signal of 1 V and 13 Hz. It is followed by a resistor connected to the source of the sample, whose drain is grounded. Back (top) gate (G1) is connected to a sourcemeter to control the gate voltage, while top (back) gate (G2) is set to a constant value using another sourcemeter. Voltage across two twBLG/hall contacts in the sample is measured by LIA.

Now the resistance across the contacts (R) is calculated as follows:

$$I = \frac{V_{LIA}}{R + 100M\Omega} = \frac{V_{AB}}{R}$$

$$R \times V_{LIA} = V_{AB} \times (R + 100M\Omega)$$

$$R = \frac{V_{AB} \times 100M\Omega}{V_{LIA} - V_{AB}}$$

In our case, $R \approx 10^8 \times V_{AB} \Omega$. The protocol for transport measurement is as follows:

- Ground all the contacts and turn on LIA and sourcemeter (set to 0 V). Open source, gate (that is to be swept) and two contacts across which resistance needs to be measured. Set the other gate to a constant value using another sourcemeter.
- Sweep the gate voltage (V_G) using sourcemeter, from 0 V to maximum, then maximum to minimum, followed by minimum to 0 V. Plot V_{AB} vs V_G during this.
- Calculate resistance using the above formula and plot R vs V_G . Later carrier density can be calculated, and resistance can be plotted against it.

4.5 Tunneling measurement

Tunneling measurement is another way of exploring the electronic properties of a heterostructure. Fig. 4.5 shows the circuit diagram for tunneling measurement in our device. The lock-in amplifier (LIA) provides AC voltage V_{LIA} and is set to 5 V. The configuration is: frequency = 13 Hz, low noise, time constant = 300ms. This is passed through a voltage divider, similar to section 4.2, reducing the voltage by 10^{-4} . It is then passed through a transformer connected to Kepco sourcemeter that adds a DC signal. This is then sent to tunnel contact in the sample and taken out from a hall contact. The current is then amplified by a pre-amplifier (10^{-5} A/V) and sent to LIA and a digital multimeter (DVM). LIA measures the differential current dI , while the DVM measures DC current I_{DC} .

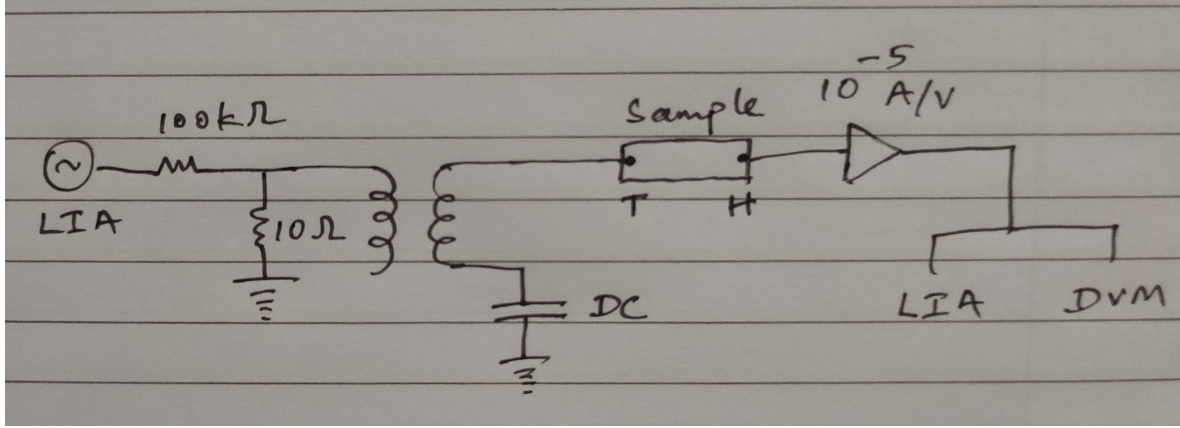


Figure 4.5: Circuit diagram for tunneling measurements in the sample. LIA is a Lock-in amplifier that provides an AC signal of $V_{LIA} = 5$ V and 13 Hz. It is followed by a voltage divider connected to a transformer. DC voltage is supplied by Kepco sourcemeter that adds to the AC voltage coming from the transformer. The AC+DC voltage is supplied to the sample through a tunnel contact T. A hall contact of the sample is then connected to LIA and a digital multimeter (DVM) through a pre-amplifier.

The protocol for tunneling measurement is as follows:

- Ground all the contacts and turn on LIA and Kepco DC source (set to 0 V). Open tunnel and twBLG contacts across which tunneling needs to be measured.
- Sweep the DC voltage (V_{DC}) using Kepco DC source, from 0 V to maximum, then maximum to minimum, followed by minimum to 0 V. Record dI from LIA and I_{DC} from DVM.
- Plot tunneling current I_{DC} vs voltage V_{DC} and tunneling conductivity dI/V_{LIA} vs voltage V_{DC} .

4.6 Stack 62

Two stacks were fabricated and measured during the course of the project, by Radhika and myself. Contact checking was done in stack 61, and during this process, the sample had electrostatic discharge, which was verified under optical microscope. Finally, stack 62 was used in our project, whose optical image is shown in fig. 4.6 and 4.7. The device structure is as described in section 3. The various contacts in the device are listed below:

- Source: 1
- Drain: 16
- twBLG/Hall contacts: 5, 6, 8, 18
- Tunnel contacts: 3, 19
- Top gate: 15
- Back gate: 1, 13

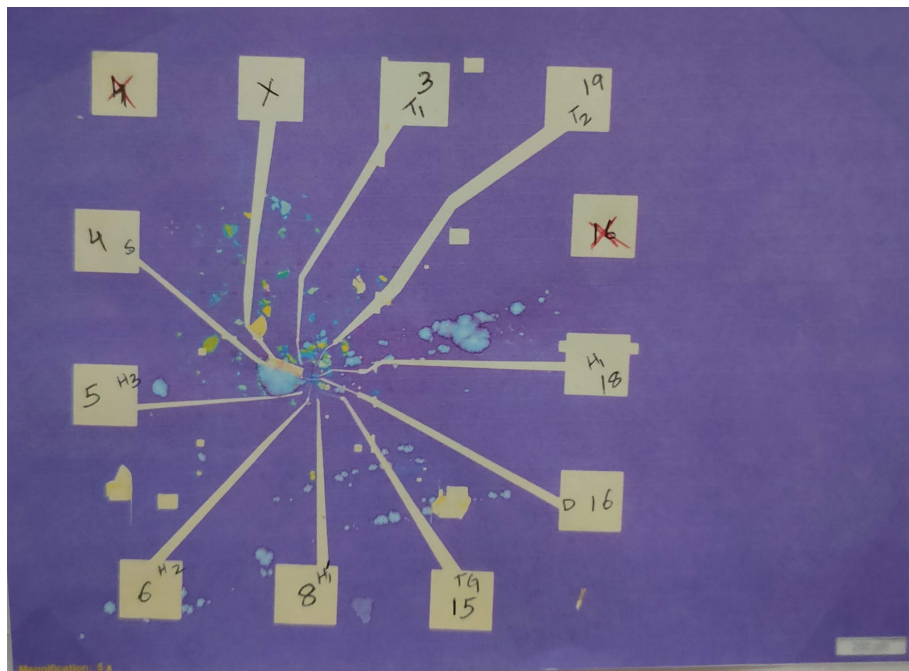


Figure 4.6: Optical image of stack 62 at 5x magnification. The scale on the right is 200 μm . All the contacts are numbered. S, D and TG represent source, drain and top gate, respectively. H1, H1', H2, H3 represent twBLG/hall contacts. T1 and T2 represent tunnel contacts. 1 and 13 are back gate contacts (not shown here as they are contacts with substrate directly).

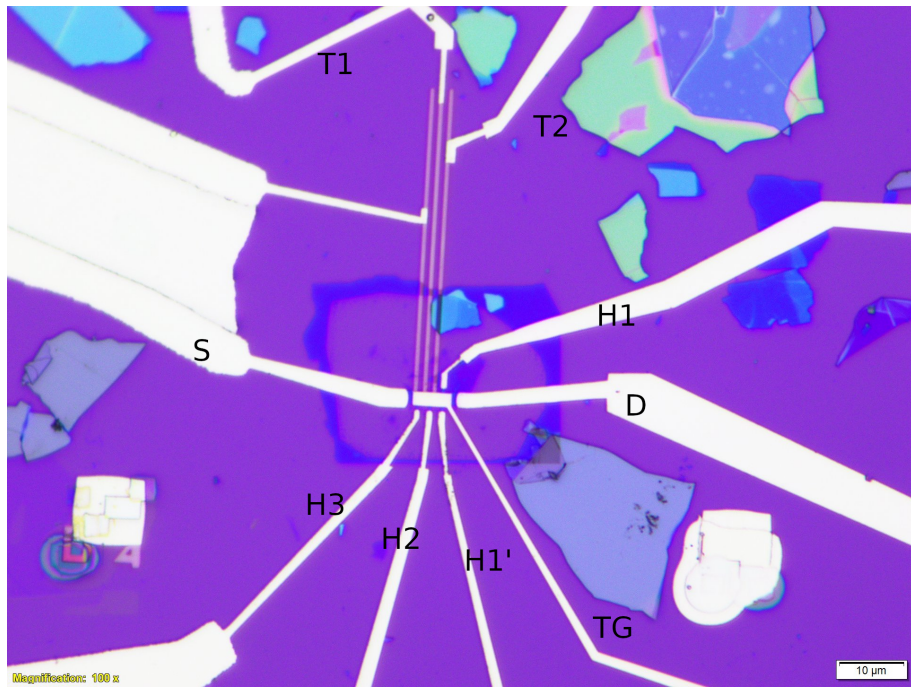


Figure 4.7: Optical image of stack 62 at 100x magnification. The scale on the right is $10 \mu\text{m}$. The nomenclature is the same as in fig. 4.6

4.6.1 Checking contacts and gate leakage

Contacts were checked using the protocol described in 4.2. V1 and V2 are voltage drops across the resistor with contact grounded and open respectively. The data noted is shown below:

Contact No.	Contact type	V1	V2	Contact status
4	twBLG/Source	97.6 μV	55.2 μV	Good
5	twBLG/Hall	97.6 μV	44.7 μV	Good
6	twBLG/Hall	97.6 μV	47.1 μV	Good
8	twBLG/Hall	97.6 μV	49.8 μV	Good
16	twBLG/Drain	97.6 μV	58.9 μV	Good
18	twBLG/Hall	97.6 μV	40.52 μV	Good
3	Tunnel	97.8 μV	55.5 μV	Bad
19	Tunnel	97.8 μV	55.3 μV	Bad

Figure 4.8: Data for checking contacts

We see that for twBLG contacts, the voltage drops by half on opening the contacts, as expected from the discussion in section 4.2. Hence, these contacts are

good and can be used in our experiment. However, for tunnel contacts, on opening the contacts, the voltage again drops by half instead of the expected 2/3 of the original value. This can be explained by considering the tunnel contacts to have very high resistance, making the effective resistance between point B and ground to be almost $10 \text{ M}\Omega$. This makes the voltage drop by half across the resistor. This shows that the tunnel contacts cannot be used in our experiment, and hence we explored only the transport properties of the device.

The reasons for high resistance in the tunnel contact could be due to various reasons:

- The tunnel hBN used in the stack could be thicker than expected (2.5 nm). As the tunneling resistance increases exponentially with hBN thickness, even if the hBN is slightly thicker, it can lead to a bad tunnel contact reading. This is the most likely reason
- The gold pad contacts could be discontinuous.
- The gold pad contacts may not be below the twBLG region.

Gate leakage was checked using the protocol described in section 4.3. The compliance is set to 3 nA. For back gate (contact 1)(contact 13 grounded), there was no overload in current seen till 35 V on the positive side and -35 V on the negative side. For top gate (contact 15), there was no overload in current seen till -10 V on the negative side, but overload was seen at 9.7 V on the positive side. Based on this, $\pm 5 \text{ V}$ was set to be the sweep limit for top gate and $\pm 30 \text{ V}$ for back gate.

4.6.2 Transport measurements and results

The tunnel contacts in the device were found to be unusable while checking the contacts. Nevertheless, we attempted to measure tunneling using the protocol described in section 4.5. We then performed transport measurement using the protocol described in section 4.4, by dipping the sample in liquid N_2 at 100 K and vacuum was created via a vacuum pump. Back gate was set at a constant value and top gate was swept between -5 V and

5V, with step size 0.01 V. This was done for three pairs of contacts - (5,6), (6,8) and (5,8) (see fig. 4.7).

First, the back gate was set to 0 V, and resistance vs top gate voltage was calculated for different contact pairs. Carrier density was calculated using the formula,

$$n = \frac{V_G \epsilon \epsilon_0}{ed} \quad (4.1)$$

where n is carrier density, ϵ is the dielectric constant of hBN (4), ϵ_0 is the permittivity of free space, e is electric charge, and d is the thickness of top hBN (15 nm). Resistance vs carrier density was plotted (see fig. 4.9). It can be seen that $V(5,6)$ and $V(6,8)$ add up to give $V(5,8)$. This is expected as they are on the same side of the sample.

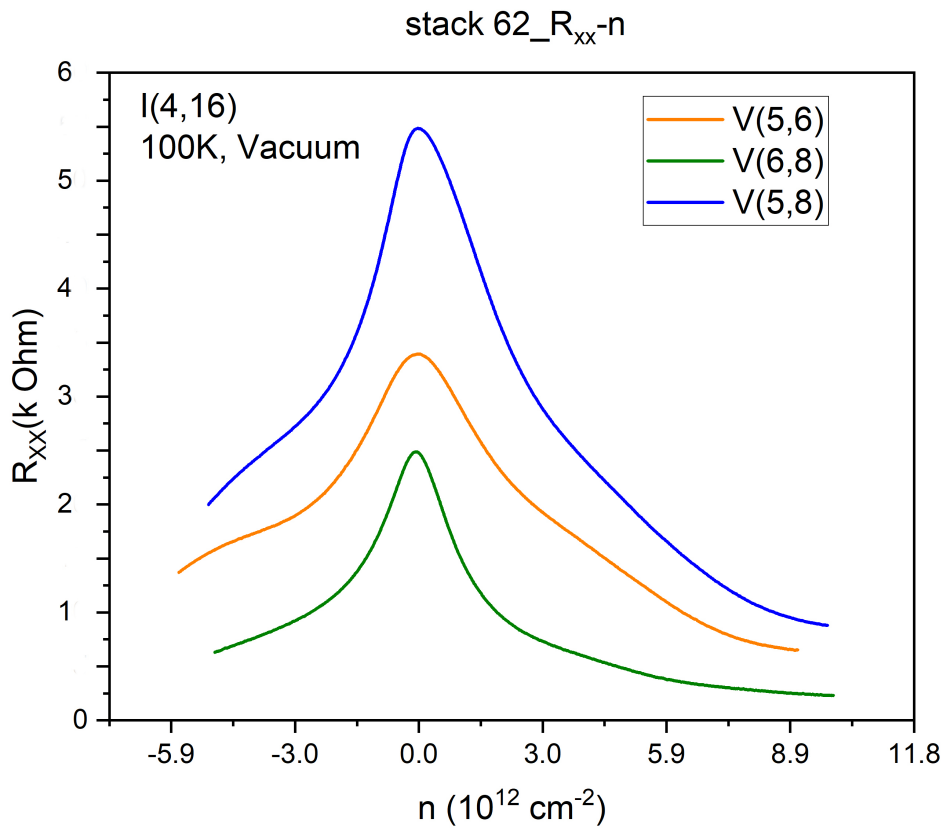


Figure 4.9: Resistance vs carrier density for different contact pairs. Back gate is set to 0 V and top gate is swept between -5 V and 5 V.

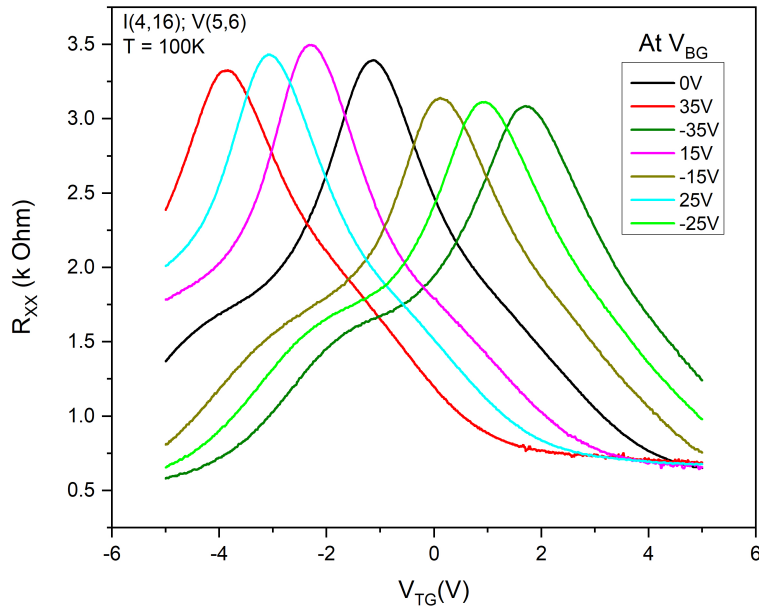


Figure 4.10: Resistance vs top gate voltage for contact pair (5,6) at different back gate voltages.

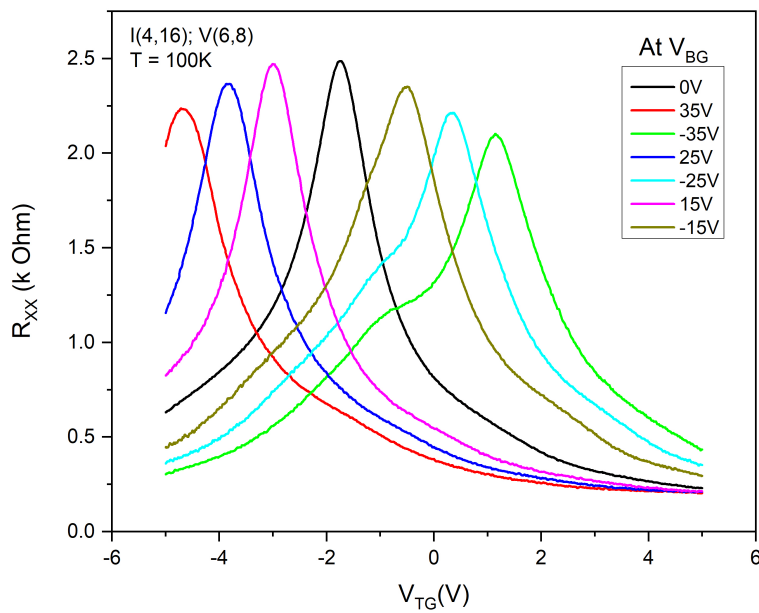


Figure 4.11: Resistance vs top gate voltage for contact pair (6,8) at different back gate voltages.

Next, the back gate was set to different voltages, and resistance vs top gate voltage was plotted for contact pairs (5,6) (fig. 4.10) and (6,8) (fig. 4.11). We can see that the resistance peak does not change much in the case of (5,6) for different back gate voltages, while it changes slightly in the case of (6,8). This suggests that the twist angle in the region between contacts 5 and 6 is small, while the twist angle between 6 and 8 could be large. This can be explained by looking at the changes to the bands on the application of a displacement field.

For Bernal-stacked bilayer, resistance increases rapidly as the displacement field increases due to the gap opening at the CNP by breaking inversion symmetry. For large-angle twBLG, resistance decreases as the displacement field increases. The electronic band of large-angle twBLG can be described by two Dirac cones displaced in reciprocal space with negligibly small interlayer coupling. Thus, the weakly coupled layers are doped with an equal amount but opposite sign of carriers as the displacement field increases, making both layers less resistive. For low angle twBLG, there is electronic transport along the network of one-dimensional topological channels that surround the alternating triangular gapped domains. Under a transverse electric field, the nearly commensurate AB and BA domains are gapped out, leaving topologically protected 1D conduction channels along their boundaries. [46]

Another feature that can be seen is small domes in the resistance graph away from the center, more visible on the hole side. Since the measurement is done at 100 K, we can't conclude much, but, this feature suggests a presence of correlated insulator state at the regions of the domes.

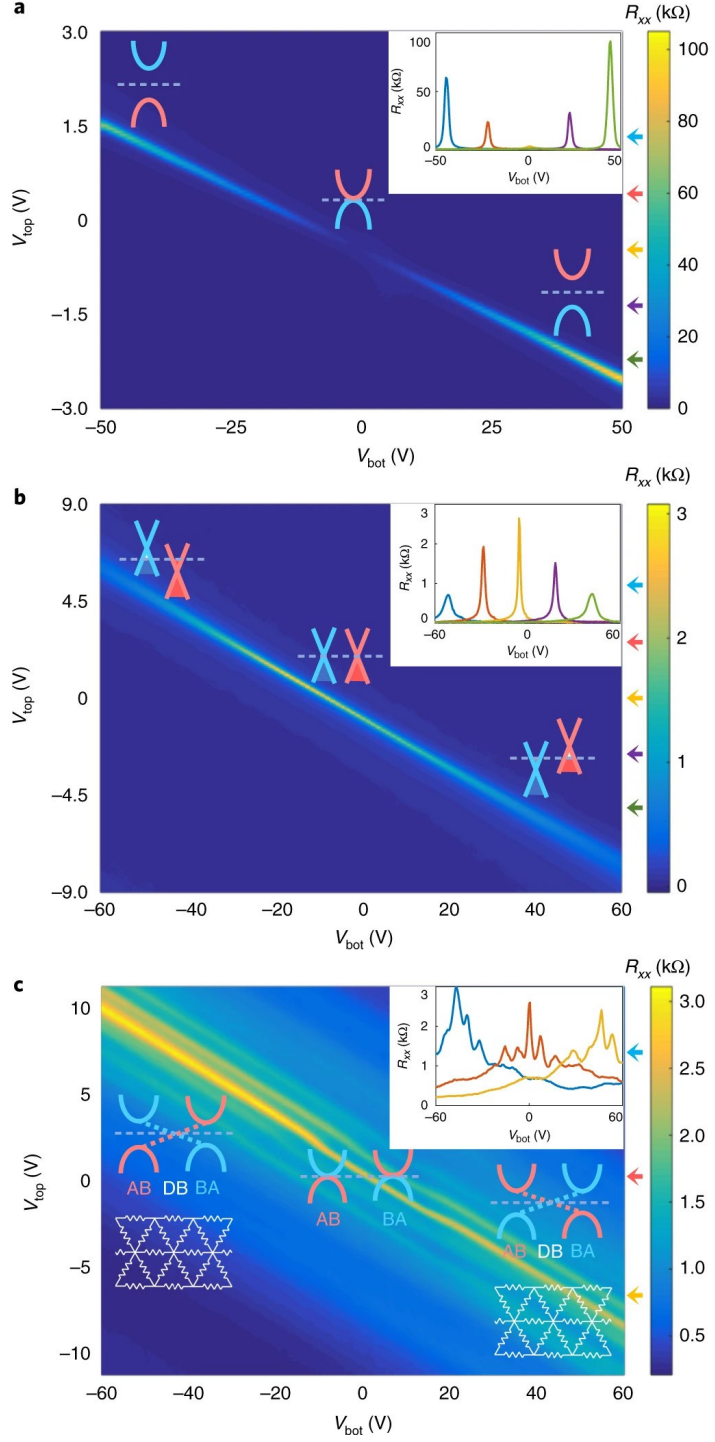


Figure 4.12: The dependence of the longitudinal resistance on top and bottom gate in (a) Bernal-stacked BLG, (b) large-angle TBG (2.8°) and (c) small-angle TBG (0.47°). The insets in the top right corner show several line cuts at fixed top-gate voltages. Schematic band structures in the inset show how the band structures change as a function of the perpendicular electric displacement field, D. The schematic diagram of the triangular network of resistors in (c) represents the current paths generated along the domain boundaries obtained by gapping out AB and BA domains with transverse electric field. DB denotes the domain boundaries. Figure adapted from [46]

Chapter 5

Conclusions

5.1 Summary

- We explored the emerging field of twistronics, through theory and paper discussions.
- We learnt fabrication of 2D heterostructures: mechanical exfoliation and transfer process
- We learnt transport and tunneling measurement in twBLG device.

5.2 Future work possible

- Fabricate more twBLG tunnel devices with different twist angles to explore their transport and tunneling properties.
- The stack which we measured is expected to have a low angle, which is being explored by performing low temperature transport and thermo-electric measurements.
- Fabricate twBLG tunnel device with WSe_2 as tunneling barrier as it is not too transparent or opaque and has a favorable band alignment with graphene.

Bibliography

- [1] Y. Cao, V. Fatemi, A. Demir, S. Fang, S. L. Tomarken, J. Y. Luo, J. D. Sanchez-Yamagishi, K. Watanabe, T. Taniguchi, E. Kaxiras, R. C. Ashoori and P. Jarillo-Herrero, ‘Correlated insulator behaviour at half-filling in magic-angle graphene superlattices,’ *Nature*, vol. 556, no. 7699, pp. 80–84, Apr. 2018 (cit. on pp. 1, 3, 10, 16–18).
- [2] Y. Cao, V. Fatemi, S. Fang, K. Watanabe, T. Taniguchi, E. Kaxiras and P. Jarillo-Herrero, ‘Unconventional superconductivity in magic-angle graphene superlattices,’ *Nature*, vol. 556, no. 7699, pp. 43–50, Apr. 2018 (cit. on pp. 1, 3, 17–20).
- [3] R. Ribeiro-Palau, C. Zhang, K. Watanabe, T. Taniguchi, J. Hone and C. R. Dean, ‘Twistable electronics with dynamically rotatable heterostructures,’ *Science*, vol. 361, no. 6403, pp. 690–693, 2018 (cit. on p. 1).
- [4] M. Serlin, C. L. Tschirhart, H. Polshyn, Y. Zhang, J. Zhu, K. Watanabe, T. Taniguchi, L. Balents and A. F. Young, ‘Intrinsic quantized anomalous hall effect in a moiré heterostructure,’ *Science*, vol. 367, no. 6480, pp. 900–903, 2020 (cit. on pp. 1, 17, 21, 22).
- [5] A. L. Sharpe, E. J. Fox, A. W. Barnard, J. Finney, K. Watanabe, T. Taniguchi, M. A. Kastner and D. Goldhaber-Gordon, ‘Emergent ferromagnetism near three-quarters filling in twisted bilayer graphene,’ *Science*, vol. 365, no. 6453, pp. 605–608, 2019 (cit. on pp. 1, 17, 21).
- [6] A. Mishchenko, J. S. Tu, Y. Cao, R. V. Gorbachev, J. R. Wallbank, M. T. Greenaway, V. E. Morozov, S. V. Morozov, M. J. Zhu, S. L. Wong, F. Withers, C. R. Woods, Y.-J. Kim, K. Watanabe, T. Taniguchi, E. E. Vdovin, O. Makarovsky, T. M. Fromhold, V. I. Fal’ko, A. K. Geim, L. Eaves and K. S. Novoselov, ‘Twist-

- controlled resonant tunnelling in graphene/boron nitride/graphene heterostructures,' *Nature Nanotechnology*, vol. 9, no. 10, pp. 808–813, Oct. 2014 (cit. on pp. 1, 3, 22–24).
- [7] N. Turner, J. T. Nicholls, E. H. Linfield, K. M. Brown, G. A. C. Jones and D. A. Ritchie, 'Tunneling between parallel two-dimensional electron gases,' *Phys. Rev. B*, vol. 54, pp. 10 614–10 624, 15 Oct. 1996. DOI: 10.1103/PhysRevB.54.10614. [Online]. Available: <https://link.aps.org/doi/10.1103/PhysRevB.54.10614> (cit. on pp. 1, 28).
- [8] U. Chandni, K. Watanabe, T. Taniguchi and J. P. Eisenstein, 'Signatures of phonon and defect-assisted tunneling in planar metal–hexagonal boron nitride–graphene junctions,' *Nano Letters*, vol. 16, no. 12, pp. 7982–7987, Dec. 2016 (cit. on pp. 1, 29, 34).
- [9] B. Hunt, J. D. Sanchez-Yamagishi, A. F. Young, M. Yankowitz, B. J. LeRoy, K. Watanabe, T. Taniguchi, P. Moon, M. Koshino, P. Jarillo-Herrero and R. C. Ashoori, 'Massive dirac fermions and hofstadter butterfly in a van der waals heterostructure,' *Science*, vol. 340, no. 6139, pp. 1427–1430, 2013 (cit. on p. 2).
- [10] M. Yankowitz, J. Xue, D. Cormode, J. D. Sanchez-Yamagishi, K. Watanabe, T. Taniguchi, P. Jarillo-Herrero, P. Jacquod and B. J. LeRoy, 'Emergence of superlattice dirac points in graphene on hexagonal boron nitride,' *Nature Physics*, vol. 8, no. 5, pp. 382–386, May 2012 (cit. on p. 2).
- [11] C. R. Dean, L. Wang, P. Maher, C. Forsythe, F. Ghahari, Y. Gao, J. Katoch, M. Ishigami, P. Moon, M. Koshino, T. Taniguchi, K. Watanabe, K. L. Shepard, J. Hone and P. Kim, 'Hofstadter's butterfly and the fractal quantum hall effect in moiré superlattices,' *Nature*, vol. 497, no. 7451, pp. 598–602, May 2013 (cit. on p. 2).
- [12] L. A. Ponomarenko, R. V. Gorbachev, G. L. Yu, D. C. Elias, R. Jalil, A. A. Patel, A. Mishchenko, A. S. Mayorov, C. R. Woods, J. R. Wallbank, M. Mucha-Kruczynski, B. A. Piot, M. Potemski, I. V. Grigorieva, K. S. Novoselov, F. Guinea, V. I. Fal'ko and A. K. Geim, 'Cloning of dirac fermions in graphene superlattices,' *Nature*, vol. 497, no. 7451, pp. 594–597, May 2013 (cit. on p. 2).

- [13] W. Yang, G. Chen, Z. Shi, C.-C. Liu, L. Zhang, G. Xie, M. Cheng, D. Wang, R. Yang, D. Shi, K. Watanabe, T. Taniguchi, Y. Yao, Y. Zhang and G. Zhang, ‘Epitaxial growth of single-domain graphene on hexagonal boron nitride,’ *Nature Materials*, vol. 12, no. 9, pp. 792–797, Sep. 2013 (cit. on p. 2).
- [14] H. Schmidt, J. C. Rode, D. Smirnov and R. J. Haug, ‘Superlattice structures in twisted bilayers of folded graphene,’ *Nature Communications*, vol. 5, no. 1, p. 5742, Dec. 2014 (cit. on pp. 2, 3).
- [15] A. K. Geim and I. V. Grigorieva, ‘Van der waals heterostructures,’ *Nature*, vol. 499, no. 7459, pp. 419–425, Jul. 2013 (cit. on p. 2).
- [16] T. Iwasaki, S. Nakaharai, Y. Wakayama, K. Watanabe, T. Taniguchi, Y. Morita and S. Moriyama, ‘Single-carrier transport in graphene/hbn superlattices,’ *Nano Letters*, vol. 20, no. 4, pp. 2551–2557, Apr. 2020 (cit. on p. 2).
- [17] R. Bistritzer and A. H. MacDonald, ‘Moiré bands in twisted double-layer graphene,’ *Proceedings of the National Academy of Sciences*, vol. 108, no. 30, pp. 12233–12237, 2011 (cit. on pp. 2, 3, 10, 11, 14–16).
- [18] K. Kim, M. Yankowitz, B. Fallahazad, S. Kang, H. C. P. Movva, S. Huang, S. Larantis, C. M. Corbet, T. Taniguchi, K. Watanabe, S. K. Banerjee, B. J. LeRoy and E. Tutuc, ‘Van der waals heterostructures with high accuracy rotational alignment,’ *Nano Letters*, vol. 16, no. 3, pp. 1989–1995, 2016 (cit. on pp. 2, 42, 49).
- [19] D. Wang, G. Chen, C. Li, M. Cheng, W. Yang, S. Wu, G. Xie, J. Zhang, J. Zhao, X. Lu, P. Chen, G. Wang, J. Meng, J. Tang, R. Yang, C. He, D. Liu, D. Shi, K. Watanabe, T. Taniguchi, J. Feng, Y. Zhang and G. Zhang, ‘Thermally induced graphene rotation on hexagonal boron nitride,’ *Phys. Rev. Lett.*, vol. 116, p. 126101, 12 Mar. 2016 (cit. on p. 3).
- [20] C. R. Woods, F. Withers, M. J. Zhu, Y. Cao, G. Yu, A. Kozikov, M. Ben Shalom, S. V. Morozov, M. M. van Wijk, A. Fasolino, M. I. Katsnelson, K. Watanabe, T. Taniguchi, A. K. Geim, A. Mishchenko and K. S. Novoselov, ‘Macroscopic self-reorientation of interacting two-dimensional crystals,’ *Nature Communications*, vol. 7, no. 1, p. 10800, Mar. 2016 (cit. on p. 3).
- [21] Y. Cao, J. Y. Luo, V. Fatemi, S. Fang, J. D. Sanchez-Yamagishi, K. Watanabe, T. Taniguchi, E. Kaxiras and P. Jarillo-Herrero, ‘Superlattice-induced insulating

- states and valley-protected orbits in twisted bilayer graphene,’ *Phys. Rev. Lett.*, vol. 117, p. 116 804, 11 Sep. 2016 (cit. on pp. 3, 49).
- [22] L.-J. Yin, J.-B. Qiao, W.-X. Wang, W.-J. Zuo, W. Yan, R. Xu, R.-F. Dou, J.-C. Nie and L. He, ‘Landau quantization and fermi velocity renormalization in twisted graphene bilayers,’ *Phys. Rev. B*, vol. 92, p. 201 408, 20 Nov. 2015 (cit. on p. 3).
- [23] A. Luican, G. Li, A. Reina, J. Kong, R. R. Nair, K. S. Novoselov, A. K. Geim and E. Y. Andrei, ‘Single-layer behavior and its breakdown in twisted graphene layers,’ *Phys. Rev. Lett.*, vol. 106, p. 126 802, 12 Mar. 2011 (cit. on p. 3).
- [24] B. Fallahazad, K. Lee, S. Kang, J. Xue, S. Larentis, C. Corbet, K. Kim, H. C. P. Movva, T. Taniguchi, K. Watanabe, L. F. Register, S. K. Banerjee and E. Tutuc, ‘Gate-tunable resonant tunneling in double bilayer graphene heterostructures,’ *Nano Letters*, vol. 15, no. 1, pp. 428–433, 2015 (cit. on pp. 3, 22, 24, 25).
- [25] G. W. Burg, N. Prasad, B. Fallahazad, A. Valsaraj, K. Kim, T. Taniguchi, K. Watanabe, Q. Wang, M. J. Kim, L. F. Register and E. Tutuc, ‘Coherent interlayer tunneling and negative differential resistance with high current density in double bilayer graphene–wse₂ heterostructures,’ *Nano Letters*, vol. 17, no. 6, pp. 3919–3925, 2017 (cit. on pp. 3, 22, 25).
- [26] G. W. Burg, N. Prasad, K. Kim, T. Taniguchi, K. Watanabe, A. H. MacDonald, L. F. Register and E. Tutuc, ‘Strongly enhanced tunneling at total charge neutrality in double-bilayer graphene-WSe₂ heterostructures,’ *Phys. Rev. Lett.*, vol. 120, p. 177 702, 17 Apr. 2018 (cit. on pp. 3, 22, 26).
- [27] F. A. Chaves, D. Jiménez, A. W. Cummings and S. Roche, ‘Model of the electrostatics and tunneling current of metal-graphene junctions and metal-insulator-graphene heterostructures,’ 2013. arXiv: 1309 . 0390 [cond-mat.mes-hall] (cit. on pp. 3, 26, 27).
- [28] A. H. Castro Neto, F. Guinea, N. M. R. Peres, K. S. Novoselov and A. K. Geim, ‘The electronic properties of graphene,’ *Rev. Mod. Phys.*, vol. 81, pp. 109–162, 1 Jan. 2009 (cit. on pp. 4–8, 12).
- [29] Y. Zhang, T.-T. Tang, C. Girit, Z. Hao, M. C. Martin, A. Zettl, M. F. Crommie, Y. R. Shen and F. Wang, ‘Direct observation of a widely tunable bandgap in

- bilayer graphene,’ *Nature*, vol. 459, no. 7248, pp. 820–823, Jan. 2009 (cit. on p. 9).
- [30] G. Li, A. Luican, J. M. B. Lopes dos Santos, A. H. Castro Neto, A. Reina, J. Kong and E. Y. Andrei, ‘Observation of van hove singularities in twisted graphene layers,’ *Nature Physics*, vol. 6, no. 2, pp. 109–113, Feb. 2010 (cit. on p. 15).
 - [31] S. Wu, Z. Zhang, K. Watanabe, T. Taniguchi and E. Y. Andrei, ‘Chern insulators, van hove singularities and topological flat bands in magic-angle twisted bilayer graphene,’ *Nature Materials*, vol. 20, no. 4, pp. 488–494, Apr. 2021 (cit. on p. 17).
 - [32] X. Lu, P. Stepanov, W. Yang, M. Xie, M. A. Aamir, I. Das, C. Urgell, K. Watanabe, T. Taniguchi, G. Zhang, A. Bachtold, A. H. MacDonald and D. K. Efetov, ‘Superconductors, orbital magnets and correlated states in magic-angle bilayer graphene,’ *Nature*, vol. 574, no. 7780, pp. 653–657, Oct. 2019 (cit. on p. 20).
 - [33] H. Polshyn, M. Yankowitz, S. Chen, Y. Zhang, K. Watanabe, T. Taniguchi, C. R. Dean and A. F. Young, ‘Large linear-in-temperature resistivity in twisted bilayer graphene,’ *Nature Physics*, vol. 15, no. 10, pp. 1011–1016, Oct. 2019 (cit. on p. 20).
 - [34] Y. Cao, D. Chowdhury, D. Rodan-Legrain, O. Rubies-Bigorda, K. Watanabe, T. Taniguchi, T. Senthil and P. Jarillo-Herrero, ‘Strange metal in magic-angle graphene with near planckian dissipation,’ *Phys. Rev. Lett.*, vol. 124, p. 076 801, 7 Feb. 2020 (cit. on p. 20).
 - [35] P. Stepanov, I. Das, X. Lu, A. Fahimniya, K. Watanabe, T. Taniguchi, F. H. L. Koppens, J. Lischner, L. Levitov and D. K. Efetov, ‘Untying the insulating and superconducting orders in magic-angle graphene,’ *Nature*, vol. 583, no. 7816, pp. 375–378, Jul. 2020 (cit. on p. 21).
 - [36] Y. Saito, J. Ge, K. Watanabe, T. Taniguchi and A. F. Young, ‘Independent superconductors and correlated insulators in twisted bilayer graphene,’ *Nature Physics*, vol. 16, no. 9, pp. 926–930, Sep. 2020 (cit. on pp. 21, 49).
 - [37] H. S. Arora, R. Polski, Y. Zhang, A. Thomson, Y. Choi, H. Kim, Z. Lin, I. Z. Wilson, X. Xu, J.-H. Chu, K. Watanabe, T. Taniguchi, J. Alicea and S. Nadj-Perge, ‘Superconductivity in metallic twisted bilayer graphene stabilized by wse2,’ *Nature*, vol. 583, no. 7816, pp. 379–384, Jul. 2020 (cit. on p. 21).

- [38] M. S. A. Bhuyan, M. N. Uddin, M. M. Islam, F. A. Bipasha and S. S. Hossain, ‘Synthesis of graphene,’ *International Nano Letters*, vol. 6, no. 2, pp. 65–83, Jun. 2016 (cit. on p. 31).
- [39] M. Yi and Z. Shen, ‘A review on mechanical exfoliation for the scalable production of graphene,’ *Journal of Materials Chemistry A*, vol. 3, no. 22, pp. 11 700–11 715, 2015 (cit. on pp. 31, 32).
- [40] M. Zastrow. ‘Meet the crystal growers who sparked a revolution in graphene electronics.’ (2019), [Online]. Available: <https://www.nature.com/articles/d41586-019-02472-0> (cit. on p. 34).
- [41] Y. Wang, Z. Su, W. Wu, S. Nie, X. Lu, H. Wang, K. McCarty, S.-s. Pei, F. Robles-Hernandez, V. G. Hadjiev and J. Bao, ‘Four-fold raman enhancement of 2d band in twisted bilayer graphene: Evidence for a doubly degenerate dirac band and quantum interference,’ *Nanotechnology*, vol. 25, no. 33, p. 335 201, Jul. 2014 (cit. on p. 36).
- [42] A. C. Ferrari, J. C. Meyer, V. Scardaci, C. Casiraghi, M. Lazzeri, F. Mauri, S. Piscanec, D. Jiang, K. S. Novoselov, S. Roth and A. K. Geim, ‘Raman spectrum of graphene and graphene layers,’ *Phys. Rev. Lett.*, vol. 97, p. 187 401, 18 Oct. 2006 (cit. on pp. 36–38).
- [43] P. Lespade, A. Marchand, M. Couzi and F. Cruege, ‘Caracterisation de materiaux carbones par microspectrometrie raman,’ *Carbon*, vol. 22, no. 4, pp. 375–385, 1984 (cit. on p. 38).
- [44] R. V. Gorbachev, I. Riaz, R. R. Nair, R. Jalil, L. Britnell, B. D. Belle, E. W. Hill, K. S. Novoselov, K. Watanabe, T. Taniguchi, A. K. Geim and P. Blake, ‘Hunting for monolayer boron nitride: Optical and raman signatures,’ *Small*, vol. 7, no. 4, pp. 465–468, 2011 (cit. on p. 38).
- [45] L. Wang, I. Meric, P. Y. Huang, Q. Gao, Y. Gao, H. Tran, T. Taniguchi, K. Watanabe, L. M. Campos, D. A. Muller, J. Guo, P. Kim, J. Hone, K. L. Shepard and C. R. Dean, ‘One-dimensional electrical contact to a two-dimensional material,’ *Science*, vol. 342, no. 6158, pp. 614–617, 2013 (cit. on p. 42).
- [46] H. Yoo, R. Engelke, S. Carr, S. Fang, K. Zhang, P. Cazeaux, S. H. Sung, R. Hovden, A. W. Tsien, T. Taniguchi, K. Watanabe, G.-C. Yi, M. Kim, M. Luskin,

E. B. Tadmor, E. Kaxiras and P. Kim, ‘Atomic and electronic reconstruction at the van der waals interface in twisted bilayer graphene,’ *Nature Materials*, vol. 18, no. 5, pp. 448–453, May 2019 (cit. on pp. 63, 64).